DOE/ET-53088-624 IFSR #624

Instability Due to Axial Shear and Surface Impedance

YU.A. TSIDULKO,[a] H.L. BERK
Institute for Fusion Studies
The University of Texas at Austin
Austin, Texas 78712
and
R. COHEN
Lawrence Livermore National Laboratory
Livermore, California 94550

September 1993

[a] *Budker Institute of Nuclear Physics*

Instability Due to Axial Shear and Surface Impedance

Yu.A. Tsidulko,[a] H.L. Berk
Institute for Fusion Studies
The University of Texas at Austin
Austin, Texas 78712
and
Ronald H. Cohen
Lawrence Livermore National Laboratory
Livermore, California 94550

Abstract

The stability of plasma flow in the scrape-off layer of a tokamak, taking into account the surface sheath impedance and the axial shear in the $\mathbf{E} \times \mathbf{B}$ flow is analyzed. An interesting stability problem arises in the limit that end plates are sufficiently far apart, so that stability can be analyzed when the plasma is taken to interact with a single end plate. As parameters are varied, windows of instability are found, and it is shown that growth rates are maximized for an insulating end plate and are also quite sensitive to the ratio of the ion diamagnetic and $\mathbf{E} \times \mathbf{B}$ drift frequencies. Mixing-length estimates of the diffusivity are comparable to experimentally observed values.

[a]Permanent address: Budker Institute of Nuclear Physics

I Introduction

Recently there have been several theoretical investigations of the stability of the scrape-off layer in a tokamak where field lines are open. Two mechanisms have been identified as the generic causes of instability: (1) the unfavorable curvature that can give rise to resistive-g instabilities[1, 2] through incomplete line tying, (2) plasma $\mathbf{E} \times \mathbf{B}$ flow in the scrape-off layer that destabilizes as a result of the interaction with the wall as described by the surface impedance.[3, 4] The latter mechanism has been shown to typically have the larger linear growth rate for typical plasma parameters.[5] In addition to the impedance drive, Kadomtsev[6] and later others,[7, 8] have shown the axial shear in $\mathbf{E} \times \mathbf{B}$ flow also gives rise to instability. The purpose of this paper is to present a description of the instability drive that accounts for flow instability due to the surface impedance and due to the axial shear. The study of axial shear effects should augment the more frequently studied radial shear problem[9, 10] which has received a great deal of interest for understanding of the edge physics in tokamaks.[11]

The structure of the paper is as follows. In Sec. II we discuss the plasma model. In Sec. III we present the double-ended solution for the problem that takes into account both the axial shear drive and the destabilization of flow from the sheath effect. In Sec. IV we discussed the stability of the single-ended problem in the case with a long Alfvén wave length. In Sec. V we consider the single-ended problem for the arbitrary wave length, using an analytic calculation for a step-function flow profile and numerical calculation for a smooth profile. In Sec. VI we present the conclusion where we summarize the relevant results of the paper. In that section we show, in terms of physical parameters, what conditions should be fulfilled to achieve a more quiescent scrape-off layer, if the flow drives described in this paper are relevant for the scrape-off layer in a tokamak. In the Appendix we consider WKB solutions of our problem.

II Plasma Model

An axial shear naturally arises on open field lines as a consequence of the variation of the electron temperature along the field line to the end-plates and because the ratio of the electrostatic potential energy $e\Phi$ to the electron temperature tends to be more slowly varying than the electron temperature. Further, as a consequence of the Spitzer law of thermal conductivity, $\chi_e \propto T_e^{5/2}$ and due to some recycling processes, most of the temperature drop arises close to the end-plates. As a consequence we assume that the variation of the electric field is on a scale length ℓ, while the distance between plates is of the scale length $L \gg \ell$. On the scale length L, the electric field is taken to be homogeneous. We assume the ion diamagnetic drift frequency to vary on the same scale. For simplicity we take all other equilibrium parameters to be constant.

In previous work,[3, 4, 5] it was assessed that typically the ideal MHD equations are justified for the response of the plasma. For simplicity we maintain this assumption in the analysis given below. We consider the model of an ideal low-beta plasma with field lines terminated by a conductor. The boundary conditions is that of a Kunkel-Guillory sheath.[12] Along the field lines the radial electric field is taken to vary.

First of all we consider a two-ended problem, and show how it approaches the limit of a one-ended problem, i.e. the problem of a semi-infinite plasma terminated by conducting plates. In the limit $k_\perp^2\, c^2/\omega_{pe}^2 \ll 1$, the equation describing the perturbed radial displacement, $\xi(s)\exp(-i\omega t + i\mathbf{k}_\perp \cdot \mathbf{r})$, is given by

$$\frac{d^2\xi}{ds^2} + \frac{(\omega - \omega_E)(\omega - \omega_E - \omega_i^*)\xi}{v_A^2} = 0 \tag{1}$$

with s the distance along a field line, $\omega_E = c\mathbf{k} \times \mathbf{b} \cdot \nabla\Phi/B$, with B the magnitude of the magnetic field, $\mathbf{b}$ its unit direction vector, $\mathbf{k}_\perp$ the wavenumber perpendicular to $\mathbf{B}$, ω the wave frequency, $\omega_i^* = \mathbf{k} \times \mathbf{b} \cdot \boldsymbol{\nabla} p_i/n_i\, m_i \omega_{ci}$ is the ion diamagnetic drift frequency, m_i the ion mass, p_i the ion pressure, $\omega_{ci} = e_i\, B/m_i\, c$ is the ion cyclotron frequency, $v_A = B/(4\pi\, n_i\, m)^{1/2}$

the Alfvén speed, and $\xi = \boldsymbol{\xi} \cdot \nabla\Phi/|\nabla\Phi|$. The plasma is taken symmetric about a mid-plane at $s = L/2$ with $0 < s < L$. The boundary conditions for the "impedance," $\xi^{-1}(s)\, d\xi(s)/ds$, at $s = 0$ and $s = L$ are respectively

$$\frac{1}{\xi}\frac{d\xi}{ds} = \begin{cases} -\dfrac{i\omega}{v_W}\,, & s = 0 \\ \dfrac{i\omega}{v_W}\,, & s = L \end{cases} \tag{2}$$

where $1/v_W = c_{sb}/v_A^2 k_\perp^2 \rho_{sb}^2$, the subscript b refers to plasma parameters adjacent to the conducting wall while the subscript 0 refers to central plasma parameters, c_{sb} is the speed with which the equilibrium ion fluid enters the sheath, often taken as the sound speed $[(T_{eb} + T_{ib})/m_i]^{1/2}$, and $\rho_{sb} = \omega_{ci}^{-1}\,(T_{eb}/m_i)^{1/2}$. For simplicity we consider the plasma density $n = \text{const}$ along the magnetic line.

In the center of the system the solution for symmetric and antisymmetric waves are respectively

$$\xi = \xi_0 \begin{Bmatrix} \cos\left[k_0(\omega)\left(s - \dfrac{L}{2}\right)\right] \\ \sin\left[k_0(\omega)\left(s - \dfrac{L}{2}\right)\right] \end{Bmatrix} \tag{3}$$

with $k_0(\omega) = (\omega - \omega_{E0})^{1/2}(\omega - \omega_{E0} - \omega_{i0}^*)^{1/2}/v_A$. Hence for $s/L \ll 1$ and $s/\ell \gg 1$, the impedance internal to the plasma is given by

$$i\,K_2 \equiv \xi^{-1}\frac{d\xi}{ds} = \begin{cases} k_0(\omega)\tan\left(k_0(\omega)\left(\dfrac{L}{2} - s\right)\right)\,, & \text{symmetric case} \\ -k_0(\omega)\cot\left(k_0(\omega)\left(\dfrac{L}{2} - s\right)\right)\,, & \text{antisymmetric case}\,. \end{cases} \tag{4}$$

We also note that if Im ω is sufficiently large (Im $\omega L \partial k_0/\partial\omega \gg 1$), that the plasma impedance condition reduces to

$$\frac{1}{\xi(s)}\frac{d\xi(s)}{ds} \longrightarrow i\,k_0(\omega)\,. \tag{5}$$

This condition allows us asymptotically to solve the problem in the domain $0 < s/\ell \ll L/\ell$, so that physically one has a response as if the two ends are "detached" from each other. We note that other mechanisms can cause effective detachment of plates distantly located from

each other. Examples include linear and nonlinear diffusive effects and cross-field propagation of the Alfvén wave due to non-MHD effects. If, for example, a wave packet bounces several times between two plates of finite cross-field width, and then propagates out of the shadow of the plates, it seems plausible to count just the finite number reflections of the wave with the plates. As a result of one reflection with the plate, the reflected wave amplitude with real frequency ω might amplify a factor A. After N reflections the wave is amplified a factor A^N. As N goes to infinity, the amplitude increases without bound. To evaluate the actual linear growth, ω must be taken in the complex plane with $\mathrm{Im}\,\omega > 0$. However, with only a finite number of reflections, there is no absolute growth, simply an amplification. To obtain absolute growth when the number of reflections are finite, one needs to look for absolute instability with only one reflection with the boundary condition given by Eq. (5).

III Solution of Two-Ended Problem

Now we need to solve the problem in the region $0 < s/L \ll 1$, with the boundary conditions given by Eq. (2) at $s = 0$ and Eq. (4) when $L/\ell \gg s/L \gg 1$. We rescale variables by $x = s/\ell$, $\Omega = \omega/\omega_{E0}$, $\Omega_E = \omega_E/\omega_{E0}$, $\Omega^* = \omega_i^*/\omega_{E0}$. Then Eq. (1) becomes

$$\frac{d^2\xi}{dx^2} + \delta^2(\Omega - \Omega_E)(\Omega - \Omega_E - \Omega^*)\xi = 0 \tag{6}$$

with $\delta = \omega_{E0}\ell/v_A$. For simplicity we take Ω^*/Ω_E as spatially constant and positive (the positiveness is generally expected under the usual equilibrium conditions). A convenient profile for Ω_E is $\Omega_E = 1 - \lambda\exp(-x)$. Then, $\Omega^* = \Omega_0^*[1 - \lambda\exp(-x)]$ and $1 - \lambda < \Omega_E < 1$. The boundary condition to Eq. (6) is $\xi^{-1}(0)\, d\xi(0)/dx = -i\Omega\delta\kappa$.

One can solve Eq. (6) straightforwardly in the limit $\delta \ll 1$. We introduce an associated equation for a variable $\tilde{\xi}$, given by

$$\frac{d^2\tilde{\xi}}{dx^2} + \delta^2(\Omega - 1)(\Omega - 1 - \Omega_0^*)\tilde{\xi} = 0 \tag{7}$$

with the constraint $\tilde{\xi}^{-1}\, d\tilde{\xi}/dx \;=\; i\,\delta\, K_2\, \ell$. Now multiplying Eq. (7) by ξ and (6) by $\tilde{\xi}$, integrating in x and subtracting the two equations, gives

$$\frac{d\xi(x)}{dx}\,\tilde{\xi}(x) - \frac{d\tilde{\xi}(x)}{dx}\,\xi(x)\Bigg|_x^0 = \delta^2 \int_0^x dx\, \xi(x)\tilde{\xi}(x)\Bigg[(\,\Omega - \Omega_E)(\Omega - \Omega_E - \Omega^*) \\ -(\Omega - 1)(\Omega - 1 - \Omega_0^*)\Bigg]\,. \tag{8}$$

Now for large x, the lower limit on the left-hand side cancels, and we obtain (using that $[\xi(0)]^{-1} d\xi(0)/dx = -i\Omega\,\delta\kappa$, $\kappa = v_A/v_W = c_{sb}/v_A k_\perp^2 \rho_{sb}^2$) the asymptotically exact result

$$\kappa\Omega + \tilde{k}(\Omega) f(\Omega) = i\delta \int_0^\infty dx\, \frac{\xi(x)\tilde{\xi}(x)}{\xi(0)\tilde{\xi}(0)}\, \left[(\Omega - \Omega_E)(\Omega - \Omega_E - \Omega^*) - (\Omega - 1)(\Omega - 1 - \Omega_0^*)\right]\,, \tag{9}$$

where $\tilde{k}(\Omega) = (\Omega - 1)^{1/2}(\Omega - 1 - \Omega_0^*)^{1/2}$ and

$$f(\Omega) = \begin{cases} -i\,\tan\left(\delta\tilde{k}(\Omega)\dfrac{L}{2\ell}\right)\,, & \text{symmetric } \xi \\ i\,\cot\left(\delta\tilde{k}(\Omega)\dfrac{L}{2\ell}\right)\,, & \text{antisymmetric } \xi\,. \end{cases}$$

If $\delta \ll 1$, $\xi(x)$ and $\tilde{\xi}(x)$ can be treated as constant, with values $\xi(0)$ and $\tilde{\xi}(0)$ respectively, in the region where the integrand in Eq. (4) is nonzero. This produces the dispersion relation

$$\kappa\Omega + \tilde{k}(\Omega) f(\Omega) = i\delta \int_0^\infty dx\, \left[(\Omega - \Omega_E)(\Omega - \Omega_E - \Omega^*) - (\Omega - 1)(\Omega - 1 - \Omega_0^*)\right]\,. \tag{10}$$

In the limit $\delta \to 0$, this result duplicates the dispersion relation for the conducting-wall-induced instability discussed in Refs. 3–5. Unless κ is small, no significantly new effect arises in Eq. (10) when δ is formally small. Let us first consider in detail $\kappa = 0$ (perfectly conducting end-plates without losses, or insulating end-plates). If $\delta L/\ell \equiv \omega_{E0}\, L/v_A \ll 1$, we recover the dispersion relation for the original Kadomtsev instability (of course with our assumed approximation $\ell/L \ll 1$). For the symmetric case, we then expand the tangent in the small argument limit and find,

$$\tilde{k}(\Omega) f(\Omega) \doteq -i\frac{L\delta}{2\ell}\,(\Omega - 1)(\Omega - 1 - \Omega_0^*)\,.$$

Taking $y = \Omega - 1$ and $\Delta\Omega_E = 1 - \Omega_E$, Eq. (10) then gives

$$y^2 - y\,\Omega_0^* = -\frac{2\ell}{L}\int_0^\infty dx\,\left[(y+\Delta\Omega_E)(y+\Delta\Omega_E-\Omega^*) - y(y-\Omega_0^*)\right] \ . \tag{11}$$

We define

$$\tilde{\Delta}\Omega_E^2 = \int_0^\infty dx\,\left[(y+\Delta\Omega_E)(y+\Delta\Omega_E-\Omega^*) - y(y-\Omega_0^*)\right] \ .$$

If y is small, as it will be from Eq. (11) when $\Omega_0^* \ll 1$, we have

$$\tilde{\Delta}\Omega_E^2 \simeq \overline{\Delta\Omega_E^2} \equiv \int_0^\infty dx\,\Delta\Omega_E^2 \ ,$$

which is a positive number. In this case we find

$$\Omega \doteqdot 1 + \frac{\Omega_0^*}{2} \pm \left[\frac{\Omega_0^{*^2}}{4} - \frac{2\ell}{L}\overline{\Delta\Omega_E^2}\right]^{1/2} \tag{12}$$

with instability due to the axial shear in the flow if $\Omega_0^{*^2} < (8\ell/L)\overline{\Delta\Omega_E^2}$ which is the Kadomtsev result (in the limit $\ell/L \ll 1$ our approximation $\widetilde{\Delta\Omega_E^2} \doteqdot \overline{\Delta\Omega^2}$ is appropriate when there is instability).

For κ finite the dispersion relation becomes

$$y^2 - y\,\Omega_0^* + \frac{2\ell}{L}\tilde{\Delta}\Omega_E^2 + i\hat{\kappa}(1+y) = 0 \tag{13}$$

with $\hat{\kappa} = 2\kappa\ell/L\delta$. To exhibit the interplay between the shear driven mode and the conducting wall instability, we take $\kappa \ll 1$ and $\Omega_0^* \ll 1$ and therefore $y \ll 1$. Then, $\tilde{\Delta}\Omega_E^2 = \overline{\Delta\Omega_E^2}$. The solution for Ω is then

$$\Omega = 1 + \frac{\Omega_0^*}{2} \pm \left[\frac{\Omega_0^{*^2}}{4} - \left(\frac{2\ell}{L}\overline{\Delta\Omega_E^2} + i\hat{\kappa}\right)\right]^{1/2} \tag{14}$$

with instability always present. The growth rate is

$$\gamma = \frac{(a^2+\hat{\kappa}^2)^{1/4}}{\sqrt{2}}\left(1 + \frac{a}{|a^2+\hat{\kappa}^2|^{1/2}}\right)^{1/2} \tag{15}$$

with $a = 2\ell\,\overline{\Delta\Omega_E^2}/L - \Omega_0^{*^2}/4$. If $\hat{\kappa}L/(2\ell\overline{\Delta\Omega_E^2}) = \kappa/(\delta\,\overline{\Delta\Omega_E^2})1$, the shear instability is subsumed by the conducting wall instability.

When $L\delta/2\ell \gg 1$, we need to use the more precise form for $f(\Omega)$. In the limit $L\delta/2\ell \gg 1$, we consider two simplifications for $f(\Omega)$. One is that $\delta\tilde{k}(\Omega)L/2\ell$ approaches its resonant values, i.e. $\delta\tilde{k}(\Omega)L/2\ell \to (n+1)\pi/2$. In this case the effect of axial shear is unimportant, and this case has been treated in detail in Ref. 5 for finite κ. The other case is treated in Sec. IV.

IV Solution of Single-Ended Problem (small δ case)

We now assume that $f(\Omega) \to i$, which is certainly valid if Im $\delta\tilde{k}(\Omega)L/2\ell \gg 1$, and, as previously mentioned, perhaps in a variety of other important cases. In this limit the dispersion relation only involves the interaction of one wall.

The dispersion relation can then be written as

$$y^{1/2}(y-\Omega_0^*)^{1/2} + \kappa + \kappa y = i\delta(\Omega_1 y + \Omega_2^2) \tag{16}$$

with $\Omega_1 \equiv 2\overline{\Delta\Omega_E} + \overline{\Delta\Omega^*}$ and $\Omega_2^2 \equiv \overline{(\Delta\Omega_E)^2} + \overline{\Delta\Omega_E\Delta\Omega^*} - \overline{\Delta\Omega_E}\Omega_0^*$ with $\Delta\Omega^* = \Omega_0^* - \Omega^*$. We note for future reference that we should only choose roots that are the analytic continuation of that branch where $\mathrm{Im}[(\Omega-1)^{1/2}(\Omega-1-\Omega_0^*)^{1/2}] > 0$ when Im $\Omega > 0$.

For arbitrary κ, Ω_1 and Ω_2, we can determine the stability boundary by examining the real and imaginary parts of Eq. (16) for purely real y. From the imaginary part, we have $y = -\Omega_2^2/\Omega_1$. [Note: if $\kappa \neq 0$, $y^{1/2}(y-\Omega_0^*)^{1/2}$ cannot be imaginary at marginal stability, as then, from the real part of Eq. (16), $y = -1$, and the product of square root terms are real for $\Omega_0^* > 0$; hence a contradiction.] Substituting this into the real part gives the stability boundary [independent of δ, within the scope of validity of Eq. (16)]

$$\kappa = \left| \left[\Omega_2^2(\Omega_2^2 + \Omega_0^*\Omega_1)\right]^{1/2} / (\Omega_2^2 - \Omega_1) \right| . \tag{17}$$

From a perturbative analysis of Eq. (16) for large κ, we readily find that the mode is

damped in that limit:

$$\kappa \operatorname{Im} y \cong -\delta\left(\Omega_1 - \Omega_2^2\right) = -\delta\overline{\Delta\Omega_E} + \overline{\Delta\Omega^*} + \overline{\Delta\Omega_E\left(\Omega_E + \Omega^*\right)} < 0 \ . \tag{18}$$

Hence, the mode is unstable for κ less than that given by Eq. (17).

If we restrict attention to equilibrium models for which Ω_E and Ω^* vary proportionally, $\Omega^* = \Omega_0^*\Omega_E$, then we have instability for

$$\kappa < \frac{\left[\overline{(\Delta\Omega_E)^2}\left(1+\Omega_0^*\right) - \Omega_0^*\overline{\Delta\Omega_E}\right]^{1/2}\left[\overline{(\Delta\Omega_E)^2} + \Omega_0^*\overline{\Delta\Omega_E}\right]^{1/2}}{\left[2\overline{\Delta\Omega_E} - \overline{(\Delta\Omega_E)^2}\right]\left(1+\Omega_0^*\right)^{1/2}} \ . \tag{19}$$

In particular, for small Ω_0^* and $\Delta\Omega_E$, this becomes

$$4\kappa^2 + \Omega_0^{*2}\overline{\Delta\Omega_E}^2 - \overline{(\Delta\Omega_E)^2} < 0 \ . \tag{20}$$

For arbitrary $\Delta\Omega_E$, it follows from Eq. (19) that the mode is completely stabilized, *i.e.* stabilized for all κ and hence all perpendicular wavenumbers, for

$$\Omega_0^* > \overline{(\Delta\Omega_E)^2} / \left[\overline{\Delta\Omega_E} - \overline{(\Delta\Omega_E)^2}\right] \ . \tag{21}$$

We consider the application of these formulas to two particular model profiles. First, for the exponential model introduced below Eq. (6), namely $\Omega_E = 1 - \lambda e^{-x}$, we have $\Omega_1 = (2+\Omega_0^*)\lambda$ and $\Omega_2 = (1+\Omega_0^*)(\lambda^2/2) - \Omega_0^*\lambda$, and the instability criterion Eq. (19) becomes

$$4\kappa^2(1+\Omega_0^*)(1-\lambda/4)^2 - \left[\frac{\lambda}{2}\left(1+\Omega_0^*\right) - \Omega_0^*\right]\left[\frac{\lambda}{2} + \Omega_0^*\right] < 0 \ , \tag{22}$$

which, for small Ω_0^* and small λ, reduces to

$$4\kappa^2 + \Omega_0^{*2} - \lambda^2/4 < 0 \ . \tag{23}$$

The complete stabilization criterion (21) is $\Omega_0^* > \lambda/(2-\lambda)$ for this model. Second, for a piecewise-constant model with $\Omega_E = 1 - \lambda$ for $0 \le x < 1$ and $\Omega_E = 1$ for $x > 1$, we have $\Omega_1 = (2+\Omega_0^*)\lambda$ and $\Omega_2 = (1+\Omega_0^*)\lambda^2 - \Omega_0^*\lambda$, and the instability criterion Eq. (19) becomes

$$2\kappa^2(1+\Omega_0^*)(1-\lambda/2)^2 - \left[\lambda\left(1+\Omega_0^*\right) - \Omega_0^*\right]\left[\lambda + \Omega_0^*\right] < 0 \ , \tag{24}$$

which for small Ω_0^* and small λ reduces to

$$2\kappa^2 + \Omega_0^{*2} - \lambda^2 < 0 \ . \tag{25}$$

The complete stabilization criterion (21) becomes $\Omega_0^* > \lambda/(1-\lambda)$.

For $\kappa = 0$, we can solve for y in a form that explicitly displays its real and imaginary parts,

$$y = \frac{\Omega_0^* - 2\delta^2\Omega_1\Omega_2^2 + i\left[\Omega_2^2\delta^2\left(4\Omega_2^2 + 4\Omega_0^*\Omega_1\right) - \Omega_0^{*2}\right]^{1/2}}{2\left(1+\delta^2\Omega_1^2\right)}$$

and we find instability criterion requires

$$\delta > \Omega_0^*/2\left[\Omega_2(\Omega_2^2 + \Omega_0^*\Omega_1)^{1/2}\right] \tag{26}$$

apparently at odds with the above analysis. The resolution is obtained by noting that marginal stability for this case occurs when $[y(y-\Omega_0^*)]^{1/2}$ in Eq. (16) is imaginary; non-zero κ invalidates this solution for marginal stability as there are then real and imaginary parts to Eq. (16) which must separately be satisfied and which are inconsistent with the square root being imaginary. When Eq. (26) predicts stability for $\kappa = 0$, for small κ there is instability with growth rate proportional to κ, whereas when Eq. (26) is satisfied, there is a finite growth rate as $\kappa \to 0$. This will be seen in the κ scans (Figs. 1b and 2b) for numerical solutions of the finite-δ dispersion relation discussed in the next section.

V Single-Ended Problem (arbitrary δ case)

We now study the arbitrary δ case for Eq. (6) with the standard boundary condition at $x = 0$ ($\xi^{-1}(0)d\xi(0)/dx = -i\Omega\delta\kappa$) and with an outgoing wave as $x \to \infty$, i.e. $\xi^{-1}(x)d\xi(x)/dx = i(\Omega-1)^{1/2}(\Omega-1-\Omega_0^*)^{1/2} \equiv i\tilde{k}(\Omega)$ (note that the branch of the square roots are chosen such that when Im $\Omega > 0$, we have a well-behaved solution as $x \to \infty$, so that Im $\tilde{k}(\Omega) > 0$; we should analytically continue this solution when Im $\Omega = 0$, which implies $\partial\Omega/\partial\tilde{k} > 0$,

i.e. outgoing group velocity, and if $\mathrm{Im}\,\Omega < 0$ then $\mathrm{Im}\,\tilde{k}(\Omega) < 0$, which is a quasi-mode solution). Consider two profiles

1. a sharp profile with

$$\begin{aligned} \Omega_E &= 1 - \lambda + \lambda H(x-1)\ ; \qquad (H(y) \equiv \text{ step function}) \\ \Omega^* &= \Omega_0^* \left[1 - \lambda + \lambda H(x-1)\right] \end{aligned} \tag{27}$$

2. a smooth profile chosen so that

$$\begin{aligned} \Omega_E &= 1 - \lambda \exp(-x) \\ \Omega^* &= \Omega_0^* \left[1 - \lambda \exp(-x)\right]\ . \end{aligned} \tag{28}$$

We will see that the dispersion relation for Eq. (27) can be analytically obtained and it is then easy to show that instability exists for the single-ended problem. However, the sharp profile, which is not very realistic, yields substantially larger growth rates than the smooth profile. For the smooth profile case we need a numerical study which is implemented by solving the Ricatti equation that can be derived from Eq. (6). In the Appendix we analytically analyze the large δ case for the smooth temperature and potential profile.

For the sharp profile we have for the solutions of Eq. (6)

$$\begin{aligned} \xi(x) &= \exp\left[i\delta\tilde{k}(\Omega)(x-1)\right]\ ; & x > 1 \\ \xi(x) &= (1-A)\exp\left[i\delta\tilde{k}_1(\Omega)(x-1)\right] + A\exp\left[-i\delta\tilde{k}_1(\Omega)x\right]\ , & 0 < x < 1 \end{aligned} \tag{29}$$

with $\tilde{k}(\Omega) = (\Omega-1)^{1/2}(\Omega-1-\Omega_0^*)^{1/2}$ and $\tilde{k}_1(\Omega) = (\Omega-1+\lambda)^{1/2}\left[\Omega-(1-\lambda)(1+\Omega_0^*)\right]^{1/2}$. The constant A is determined by applying the boundary condition at $x=0$ and the continuity of derivatives at $x=1$. This procedure leads to the dispersion relation

$$\begin{aligned} &\left(\tilde{k}_1(\Omega) - \kappa\Omega\right)\left(\tilde{k}_1(\Omega) - \tilde{k}(\Omega)\right)\exp\left(2i\delta\tilde{k}_1(\Omega)\right) \\ &\quad = \left(\tilde{k}_1(\Omega) + \tilde{k}(\Omega)\right)\left(\tilde{k}_1(\Omega) + \kappa\Omega\right)\ . \end{aligned} \tag{30}$$

Various plots of the solutions of Eq. (30) are shown in Figs. 1–4. All plots are for $\lambda = 0.7$. The most unstable case occurs for small κ. In Fig. 1a we plot $\mathrm{Re}\,\Omega$ vs. δ and in Fig. 1b we

plot Im Ω vs. δ for $\kappa = 0$ and various values of Ω_0^*. For these cases δ needs to exceed a critical threshold value to produce instability. The maximum growth rate peaks for Im $\Omega \approx 0.2$ for $\delta \approx 1.5$. The growth rate is largest for the smallest values of Ω_0^*. The growth rate vanishes for $\Omega_0^* = 2.33$.

In Fig. 2 we plot a similar graph for $\kappa = .166$. In comparing the two curves we see a decrease in the maximum growth rate with κ and Ω_0^*. Further we note that there is a curve where Im $\Omega = 0$ for all δ. The condition for such marginal curves is found by setting each side of Eq. (30) separately to zero, and one finds

$$\kappa = \left[\frac{\lambda^2}{(2-\lambda)^2}\left(1+\frac{\Omega_0^*}{2}\right)^2 - \frac{\Omega_0^{*2}}{4}\right]^{1/2} \Big/ (1+\Omega_0^*)^{1/2} \equiv \kappa_{cr} \ . \tag{31}$$

For $\kappa < \kappa_{cr}$, and $\kappa \neq 0$, the system is unstable for small δ-values, but stabilizes for δ sufficiently large. The $\kappa = 0$ case is slightly different in that it requires a threshold δ to destabilize and then the unstable spectrum doesn't stabilize at large δ. For $\kappa > \kappa_{cr}$, the system is stable for small δ, but can destabilize at larger δ. These aspects are illustrated in Fig. 3a where $\kappa = .414$ and in Fig. 3b where $\kappa = .580$. In Fig. 3a we see that the small Ω_0^* curves are unstable, but stabilize at a critical δ value (where $2\delta\tilde{k}_1(\Omega) = n\pi$ with n an integer). As δ increases, a given curve goes through stable and unstable bands. For $\kappa > \kappa_{cr}$, the curves are stable for small δ, but have bands of instability as δ increases. In Fig. 3b, where $\kappa = .580$, we have stability for all Ω_0^* values if δ is sufficiently small, and bands of instability arise as δ increases.

The instability spectrum can become fairly complicated, and it is even possible to have more than one unstable mode for the same parameters, as shown in Fig. 4.

It is clear that the most unstable region arises from $\delta \approx 1$ when κ and Ω_0^* are not too large. Though there are broad bands of instability for the larger δ cases, the maximum growth rates for these cases are nearly an order of magnitude less than the small κ^*, Ω_0^* cases.

We can compare the smooth profile model (we keep $\lambda = 0.7$) with the sharp profile model. Figure 5 shows a scan of Ω vs. δ for $\Omega_0^* = 0$ and various values of κ and Fig. 6 shows a scan of Ω vs. δ for $\kappa = 0$ for various values of Ω_0^*. It is clear that the smooth profile gives weaker instability than the sharp profile, although qualitative tendencies are similar. The maximum growth rate for the smooth profile is Im $\Omega \simeq 0.1$ which is $\sim 1/2$ the steep profile result. Small δ stabilization (for $\Omega_0^* = 0$) occurs for $\kappa \simeq .2$, whereas in the steep profile case $\kappa = 0.539$ is needed for the small δ stability. When $\kappa = 0$, the steep profile requires $\Omega_0^* \approx 1.0$ for the maximum growth rate to be reduced to half the maximum value of the $\Omega_0^* = 0$ case, while the smooth profile requires $\Omega_0^* \approx 0.5$ for the maximum growth rate to be reduced to half the $\Omega_0^* = 0$ case. Hence, we see that parameter widths for instability are significantly narrowed for the smooth profile, compared to the sharp case.

As with the steep profile, instability bands are to be expected in the large δ limit. The instability bands are given by Eqs. (A18) and (A19) of the appendix. The similar result, using linear expansion of the profile and solution of the Weber equation, was obtained. A stability band is given by Eq. (A32) of the appendix. This formulas qualitatively correlates with Figs. 5b and 7. In Fig. 5b we see that as κ increases the stability band begins at smaller δ, while Fig. 7 shows that as κ increases, the stability band terminates at smaller δ values. Also observe that in Fig. 7 the growth rates are fairly low. Hence the most interesting region remains $\delta \approx 1$.

VI Implications of Instability

To assess the implications of instability, we take the results of the smooth profile. We assume that a plausible diffusion coefficient is

$$D \sim \frac{\text{Im}\,\omega}{k_\perp^2} \exp(-\delta\psi) \ , \tag{32}$$

where Im $\omega/k_\perp^2$ is the usual mixing length result, and the exponential factor is the tunneling factor between the instability that is generated in the presheath and the rest of the plasma edge, which receives the radiation from the presheath. The attenuation constant ψ is given by Eq. (A16) in the Appendix. Of course this mixing length estimate is an extremely rough criterion, especially if Im $\omega \ll k_\perp^2 \frac{\partial^2 \mathrm{Re}\,\omega}{\partial k_\perp^2}$, but as a first assessment we shall maintain this assumption.

If we normalize D to the parameters of our theory, we find,

$$D = \Gamma \frac{v_A^2 \rho_{sb}^2}{c_{sb}\, l} \ , \tag{33}$$

where $\Gamma = \mathrm{Im}\ \Omega\, e^{-\delta\psi} \kappa\delta$.

If one now looks for the maximum of this expression as a function of κ and δ, one finds that except for unrealistically large δ values, this expression does not maximize. On the other hand, we need to have the following inequalities to be valid

$$k_\perp^2 \rho_{sb}^2 T_{e0}/T_{eb} \ll 1 \ ,$$

$$k_\perp^2 > k_\theta^2$$

and

$$(k_\perp^2 - k_\theta^2) L_T^2 > 1 \ ,$$

where L_T is the electron temperature radial scale length.

To use a reasonable set of parameters we apply a constraint that would apply under self-consistent conditions. Namely, as in Ref. 5, we note that the width of the scrape-off layer is determined by the balance between cross field diffusion and axial end loss. This gives the relation

$$\frac{D}{L_T^2} \simeq \frac{\Lambda c_{sb}}{L} \ ,$$

where L is the overall length of an open field line in the tokamak edge, $\Lambda = e\Phi/T_{e0} \simeq 4$ and c_{sb} is the sound speed. Hence

$$L_T^2 \simeq \frac{DL}{\Lambda c_{sb}} \,. \tag{34}$$

We now note that the parameter δ can be related to L_T or D, by

$$\delta^2 \equiv \frac{\omega_{E0}^2 l^2}{v_A^2} = \left(\frac{ck_\theta \Lambda T_{e0} l}{eB\, L_T\, v_A}\right)^2 \simeq (k_\theta\, \rho_{sb})^2 \frac{\Lambda^3\, l^2\, c_{sb}\, v_{Tb}^2}{D\, L\, v_A^2} \frac{T_{e0}^2}{T_{eb}^2} \,, \tag{35}$$

where $v_{Tb} = \sqrt{T_{eb}/m_i}$ and $\rho_{sb} = v_{Tb}/\omega_{ci}$. Further $k_\perp^2 \rho_{sb}^2$ is given in terms of κ as,

$$k_\perp^2 \rho_{sb}^2 \simeq \frac{c_{sb}}{v_A \kappa} \,. \tag{36}$$

Thus, with the condition $k_\theta^2/k_\perp^2 < 1$, and Eq. (33) for D, we obtain the condition,

$$\frac{k_\theta^2}{k_\perp^2} = \frac{C_1}{C_2} < 1 \,, \tag{37}$$

with

$$C_1 = \delta^3 \kappa^2 \,\mathrm{Im}\, \Omega\, e^{-\delta\psi} \tag{38}$$

(which depends on the dimensionless parameters of our calculation) and

$$C_2 = \frac{\Lambda^3\, l^3}{L \rho_{sb}^2} \frac{v_{Tb}^2 c_{sb}^3}{v_A^5} \frac{T_{e0}^2}{T_{eb}^2} \tag{39}$$

(which depends only on experimental parameters). Then we calculate the following function

$$\Gamma_m(C_2) = \max_{\delta,\kappa} \Gamma(\delta,\kappa)\Big|_{C_1(\delta,\kappa)\le C_2} \,. \tag{40}$$

The result for Ω_0^* varying from 0 to 0.7 is shown in Fig. 8. The function $\Gamma_m(C_2)$ increases and then becomes constant (except for the case with $\Omega_0^* = 0$). It arises because the function $\Gamma(\delta,\kappa)$ has a local maximum (arising from the moderate-δ, small-κ instability). There is no global maximum, because for large κ we have instability again, but for physically interesting parameters the restriction $C_1 < C_2$ excludes κ's large enough that Γ exceeds the local maximum value. Hence, the large-κ instability band does not influence the plots.

Let us now also make similar self-consistent estimates for the insulating end-wall, when κ equals zero and the relation given by Eq. (36) is absent. Hence, we can choose $k_\perp \sim k_\theta$ for any value of the parameters. Using Eqs. (32), (34) and (35), we obtain

$$L_T^4 \simeq L\, l\, \rho_{sb}^2 \frac{\Lambda v_{Tb}^2\, T_{e0}^2\, \mathrm{Im}\, \Omega e^{-\delta\psi}}{\delta v_A\, c_{sb}\, T_{eb}^2} \,. \tag{41}$$

and

$$D \simeq \rho_{sb}^2\, v_{Tb} \frac{T_{e0}}{T_{eb}} \sqrt{\frac{\Lambda^3\, l\, c_{sb}\, \mathrm{Im}\, \Omega e^{-\delta\psi}}{\delta L\, v_A}} \,. \tag{42}$$

We choose the following values of the experimental parameters, $B = 2\,\mathrm{T}$, $T_{eb} = 25\,\mathrm{eV}$, $T_{e0}/T_{eb} = 5$, $n = 10^{13}\,\mathrm{cm}^{-3}$, $L = 40\,\mathrm{m}$, $l = 2\,\mathrm{m}$, $c_{sb} = v_{Tb}$ and $\Lambda = 4$.

Typical results are the following:

If $\Omega_0^* = 0$ then the most unstable values of our dimensionless parameters for a conducting end-wall are $\delta = 2$, $\kappa = 0.08$, Re $\Omega = 0.77$, Im $\Omega = 0.047$, $k_\perp^2 \rho_{sb}^2 T_{e0}/T_{eb} = 0.2$, $(k_\perp^2 - k_\theta^2) L_T^2 = 17$. Then the diffusion coefficient equals $D = 1\, m^2/\,\mathrm{sec}$ and the radial scale length is $L_T = 1.4\,\mathrm{cm}$.

In the case with insulating end-wall and $\Omega_0^* = 0$, the small values of δ are most unstable: $\delta = 0.2$, $\kappa = 0$, Re $\Omega = 0.988$, Im $\Omega = 0.045$, $k_\perp^2 \rho_{sb}^2 T_{e0}/T_{eb} = 6 \times 10^{-3}$, $k_\perp^2\, L_T^2 = 13$. Then the diffusion coefficient equals $D = 3.2\,\mathrm{m}^2/\,\mathrm{sec}$, and the radial scale length is $L_T = 2.5\,\mathrm{cm}$. We see that the insulating end wall case has a larger diffusion coefficient, at least for our choice of mixing-length estimate. (Note, for example, that replacing $k_\perp^2$ by $k_r^2 = k_\perp^2 - k_\theta^2$) in the mixing-length estimate would increase the diffusion coefficient for the conducting-wall case.)

If $\Omega_0^* = 0.5$ then the most unstable values of our dimensionless parameters are $\delta = 4$, $\kappa = 0.028$, Re $\Omega = 0.83$, Im $\Omega = 0.02$, $\psi = 0.24$, $k_\perp^2 \rho_{sb}^2 T_{e0}/T_{eb} = 0.6$, $(k_\perp^2 - k_\theta^2) L_T^2 = 37$, then the diffusion coefficient equals $D = 0.1\, m^2/\,\mathrm{sec}$, and the radial scale length is $L_T = 0.5\,\mathrm{cm}$. For the insulating end-wall and $\Omega_0^* = 0.5$ we find: $\delta = 2$, $\kappa = 0$, Re $\Omega = 0.956$, Im $\Omega = 0.049$, $\psi = 0.6$, $k_\perp^2 \rho_{sb}^2 T_{e0}/T_{eb} = 0.1$, $k_\perp\, L_T^2 = 42$. Then the diffusion coefficient equals $D = 0.6\, m^2/\,\mathrm{sec}$, and the radial scale length is $L_T = 1.1\, cm$.

Finally, we exhibit the dependencies of D and L_T on Ω_0^* for the experimental parameters given above in Fig. 9.

We note that, for any fixed set of parameters, the insulating wall case is always more unstable than the conducting-wall case. This must be so as the insulating boundary is not as constrained, and is clearly seen in the results shown in Fig. 5. It might appear that the results quoted three paragraphs above contradict this conclusion; however, the growth rates presented for the conducting and insulating cases each correspond to a maximization of the diffusion coefficient (rather than the growth rate), and in fact occur for quite different values of δ.

The most important parameter for the instability analyses is Ω_0^*, which is a measure of the effect of FLR stabilization. If $\Omega_0^* > 0.7$ the instability is very weak and if $\Omega_0^* > \lambda/(1-\lambda)$, the axial shear is stable. Roughly $\Omega_0^* \sim \omega_i^*/(\Lambda\omega_e^*)$ and hence if $T_i < \Lambda T_e$, with $\Lambda \simeq 4$, relatively strong instability can be expected. However, as T_i/T_e increases, the strength of the instability rapidly weakens.

It is interesting to note that some experimental data indicates that the observation of the L-H-mode transition, is accompanied by increase of T_i/T_e. Perhaps this observation is an indication of the relevance of our mechanism to this important experimental observation. Thus it may be that the decrease in fluctuations is associated with an increase in FLR term $\propto T_i/T_e$ at the edge, which weakens the instability described here.

Finally we should note, that the quantitative predictions of our theory are sensitive to the scale and shape of the axial electron temperature profile, which are dependent upon the recycling processes near the end-wall. More careful study is needed of realistic experimental profiles so that a more careful correlation of our theory with experiment can be made.

Acknowledgments

We thank D.D. Ryutov, N. Mattor and X.Q. Xu for helpful discussions. This work was performed in part under the auspices of the U.S. Department of Energy by the University of Texas under Contract No. DE-FG05-80-ET-53088 and by Lawrence Livermore National Laboratory under Contract No. W7405-Eng-48.

Appendix — Solution of Single-Ended Problem (large δ case)

The mathematical problem is to connect the solution of equation

$$\frac{d^2\xi}{dx^2} + k_{\|}^2(x,\Omega)\xi = 0 \ , \tag{A1}$$

at $x = 0$, where the impedance is

$$\frac{1}{\ell\,\xi(0)}\frac{d\xi(0)}{dx} = -\frac{i\omega}{v_W} \equiv -\frac{i\Omega\,\delta\kappa}{\ell} \ , \tag{A2}$$

to the region $L/2\ell \gg s/\ell \gg 1$, where the impedance is given by Eq. (4). The coefficient $k_{\|}^2$ in Eq. (A1) denotes following expression

$$k_{\|}^2 = \delta^2(\Omega - \Omega_E)(\Omega - \Omega_E - \Omega^*) \ . \tag{A3}$$

We then need to describe the eigenfunctions in the finite s/l region. For the large δ case we can use the WKB approximation to obtain analytic insight. In fact two different approaches will be described here. In the first we use a direct WKB technique where connection formula are used to piece together regions where the WKB approximation is locally invalid. The second method is to approximate the differential equation in the region $s/l \ll 1$ as a Weber equation. For large δ, the WKB solution of the Weber equation overlaps with the WKB approximation of the original equation, when $\Omega_0^* \ll 1$ and $\Omega - \Omega_E(0) \ll 1$. With these approximations the solution of the Weber equation for large δ is an accurate approximation of the original equation.

First we describe the direct WKB technique. The single-ended problem may be understood in the following way. Near the end-wall, let us consider a WKB solution of the form

$$\xi = \frac{A_1}{k_{\|1}^{1/2}}\exp\left(i\int_0^x k_{\|1}\,dx'\right) + \frac{A_2}{k_{\|2}^{1/2}}\exp\left(i\int_0^x k_{\|2}\,dx'\right) \ , \tag{A4}$$

where $k_{\|1,2}$ are two roots of Eq. (A3). In order to derive the marginal stability condition, we assume that Im $\Omega = 0$, $k_{\|j}(x,\Omega)$ is real for x sufficiently small, and the outgoing wave (with respect to the wall at the point $x = 0$) corresponds to the first term in Eq. (A4) which is taken to have a positive group velocity

$$\left[\frac{\partial}{\partial\Omega}k_{\|1}(x,\Omega)\right]^{-1} > 0 \ . \tag{A5}$$

Using the boundary condition Eq. (A2) we find the reflection coefficient at the wall $|r_w|^2 \equiv \left|\frac{A_1}{A_2}\right|^2$ is given by

$$r_w = \frac{k_{\|w} - \delta\Omega\kappa}{k_{\|w} + \delta\Omega\kappa} \tag{A6}$$

and $k_{\|w} = k_{\|1}(0,\Omega)$.

In addition to the end wall there is wave reflection from the tunneling region in the sheath. To have such a tunneling region certain conditions in Ω need to be satisfied. Consider Fig. 10 where $E_1(x) \equiv \Omega_E(x)$ and $E_2(x) \equiv \Omega_E(x) + \Omega^*(x)$ are plotted. It is clear that for real Ω the regions of propagation of the WKB waves [i.e. $k_{\|}^2(x,\Omega) \equiv \delta^2(\Omega - \Omega_E(x))(\Omega - \Omega_E(x) - \Omega^*(x)) > 0$] occur for Ω and x values above and below both the two curves shown in the figure. An eigenmode at fixed Ω can have both propagating and evanescent regions. If

$$\Omega_2 < \Omega < \Omega_3 \ , \tag{A7}$$

where $\Omega_2 \equiv \Omega_E(0) + \Omega^*(0)$ and $\Omega_3 \equiv \Omega_E(\infty) = 1$, the propagating regions lie in the interval $0 < x < x_1$ (where $\Omega > \Omega_E(x) + \Omega^*(x)$) and the interval $x > x_2$ (where $\Omega < \Omega_E(x)$). The points x_1 and x_2 are indicated in Fig. 10, and they are the turning points, i.e., where $k_{\|}^2(x,\Omega) = 0$. Then in the region $0 < x < x_1$, one can have waves propagating in both directions in the form of Eq. (A4). These waves are evanescent in the interval $x_1 < x < x_2$, while for $x > x_2$ the WKB solution has only a single amplitude, with $k_{\|} = k_{\|1}(x,\Omega)$ where $k_{\|1}(x,\Omega)$ satisfies Eq. (A5). A standing wave can then be established if near $x = 0$ the incoming wave of amplitude A_2 reflects at the Kunkel-Guillory sheath, with the reflection

coefficient given by Eq. (A6) so that $A_1 = r_w A_2$. The outgoing wave then reflects at the turning point x_1 with a reflection coefficient r_t, and we then require

$$A_2 \exp\left(i \int_0^{x_1} k_{\|2}\, dx'\right) = r_t A_1 \exp\left(i \int_0^{x_1} k_{\|1}\, dx'\right) = r_t r_w \exp\left(-i \int_0^{x_1} k_{\|2}\, dx'\right) A_2$$

where $k_{\|2}(x') = -k_{\|1}(x')$ is used. Thus, if r_t can be determined, we have the dispersion relation

$$1 - r_t r_w \exp\left(-2i \int_0^{x_1} dx'\, k_{\|2}(x', \Omega)\right) = 0 \ .$$

By noting that $\int_0^{x_1} dx'\, k_{\|2}(x', \Omega)$ is real at marginal stability (because Ω is real and we are in the propagating interval), we observe that marginal stability requires

$$|r_w r_t|^2 = 1 \ . \tag{A8}$$

We note that $|r_t|^2$ can be calculated extremely accurately using techniques described by Heading[14] which we will shortly discuss below.

If Ω does not lie in the region given by Eq. (A7), we will not find a marginal mode. To confirm this assertion we note that if $\Omega < \Omega_1 \equiv \Omega_E(0)$ or $\Omega > \Omega_4 \equiv \Omega_E(\infty) + \Omega^*(\infty)$ there are no turning points to produce the reflection coefficient r_t. In this case the wave at infinity has to have an ingoing, as well as an outgoing component, which is not an acceptable boundary condition at infinity. In the range $\Omega_1 < \Omega < \Omega_2$, we have an evanescent region for $0 < x < x_2$ (in this case $k_{\|j}(x, \Omega)$ is imaginary at $x = 0$), which (along with the condition of outgoing waves for $x \to \infty$) guarantees that one the solutions given by Eq. (A4) is exponentially smaller than the other near $x = 0$. As in this case $|r_w| = 1$, which implies $|A_1| = |A_2|$ we have incompatibility, thus no solution. Finally, in the range $\Omega_3 < \Omega < \Omega_4$, waves do not propagate at infinity. This implies $|r_t| = 1$. However, as $|r_w| < 1$, we cannot satisfy the marginal condition $|r_w r_t| = 1$.

Now let us consider the behavior of the wall reflection coefficient $|r_w|^2$ in the range defined by Eq. (A7). In Figs. 11a and 11b we plot $\ln |r_w|^2$ vs. $\mathrm{Re}\,\Omega$ with various values of κ. It is easy

to check analytically, that for $\kappa > 0$ that the wall reflection coefficient is always less than unity and approaches unity when either $\kappa \to 0$ or $\kappa \to \infty$. Hence, to achieve the marginal stability given by Eq. (7), we need the reflection coefficient from the tunneling region $|r_t|$ to be greater than unity. Perhaps surprisingly, the reflection coefficient $|r_t|$ in this problem is indeed larger than unity. To find it, let us obtain the relations between the wave amplitudes, using standard WKB techniques.[14]

For the tunneling problem we consider the solution given by Eq. (A4) between the wall and the tunneling region, while for $x \to \infty$ the solution has the form

$$\xi = \frac{A_\infty}{k_{\|\infty}^{1/2}} \exp\left(i \int_{x_2}^{x} k_{\|\infty}\, dx\right) . \tag{A9}$$

To apply Heading's conventions,[14] we first choose a positive root of Eq. (A3) $k_{\|\infty} > 0$. Then following Heading, the ratios between wave amplitudes are

$$\left|\frac{A_\infty}{A_p}\right|^2 = \frac{q}{1+q} \tag{A10}$$

where

$$q = \exp\left(-2\left|\int_{x_1}^{x_2} k_{\|}\, dx\right|\right) \tag{A11}$$

and

$$\left|\frac{A_n}{A_p}\right|^2 = \frac{1}{1+q} . \tag{A12}$$

For real Ω, $k_{\|}^2(x,\Omega)$ is positive above the curve $\Omega = \Omega_E(x) - \Omega^*(x) = 0$ and below the curve $\Omega - \Omega_E(x) = 0$. The subscript "p" corresponds to the choice of the $k_{\|}$ root in Eq. (A4), where $k_{\|p}$ is positive. Similarly, the subscript "n" corresponds to the choice where $k_{\|n}$ is negative. Note, the expressions given in Eqs. (A10) and (A12) are valid even if the turning points are not separable.

Equations (A10) and (A12) are also valid for the solution that is the complex conjugate of the one we have considered, because $k_{\|}^2$ has real values for real x and real Ω. Now we note, that for our case of interest the outgoing wave solution (which for $x \to \infty$ and $\Omega_2 < \Omega$

has $\frac{\partial}{\partial\Omega} k_{\|}(x,\Omega) > 0$ but $k_{\|} < 0$) is complex conjugate to the solution given by Eq. (A9). By the similar arguments it follows, that the A_1 term on the right side of Eq. (A4) is complex conjugate to the expression $\frac{A_n}{k_{\|n}^{1/2}} \exp\left(i \int_0^x k_{\|n}\, dx'\right)$ while the A_2 term is complex conjugate to the expression $\frac{A_p}{k_{\|p}^{1/2}} \exp\left(i \int_0^x k_{\|p}\, dx'\right)$. Hence, using Eqs. (A10) and (A12), we can write the transmission and reflection coefficients through the tunneling region as

$$|t_t|^2 \equiv \left|\frac{A_\infty}{A_1}\right|^2 = \left|\frac{A_\infty^*}{A_p^*} \cdot \frac{A_p^*}{A_n^*}\right|^2 = q \tag{A13}$$

and

$$|r_t|^2 \equiv \left|\frac{A_2}{A_1}\right|^2 = \left|\frac{A_p^*}{A_n^*}\right|^2 = 1 + q\ . \tag{A14}$$

Thus the reflection coefficient is greater than unity because of the opposite signs of $k_{\|}$ and the group velocity of the outgoing wave for $x \to \infty$. In terms of the notation given in Ref. 15, it means that the outgoing wave has negative cofactor σ while the waves between the end-wall and the tunneling region have positive cofactors; as a result the conservation rule appears as $|r_t|^2 - |t_t|^2 = 1$.

The expression in Eq. (A11) for q may be rewritten into the form

$$q = \exp(-\delta\psi)\ , \tag{A15}$$

where ψ for our standard smooth profile is

$$\psi \equiv 2 \int_{x_1}^{x_2} |(\Omega - \Omega_E)(\Omega - \Omega_E - \Omega_0^*)|^{1/2} dx = \frac{2\,\Omega^2 \Omega_0^{*2}}{(1-\Omega)(1+\Omega_0^*)^{3/2}} \int_0^1 \frac{\sqrt{z(1-z)}}{1+az}\, dz \tag{A16}$$

with

$$a = \frac{\Omega\Omega_0^*}{(1-\Omega)(1+\Omega_0^*)}\ .$$

The integral in Eq. (A16) may be written as the following interpolation formula, that connects the asymptotic values for large and small a,

$$\int_0^1 \frac{\sqrt{z(1-z)}}{1+az}\, dz \simeq \frac{\pi}{8\left[1+(a/4)^{7/10}\right]^{10/7}}\ . \tag{A17}$$

In Fig. 12 we have plotted $\ln |r_t|^2$ vs. $\mathrm{Re}\,\Omega$ in the range $\Omega_2 < \mathrm{Re}\,\Omega < \Omega_3$ with various values of δ and $\Omega_0^* = 0.5$. For comparison in Fig. 13 we have plotted, as a function of $\mathrm{Re}\,\Omega$, $\ln |r_s|^2$ for the sharp profile case (see Eq. (27)). This coefficient does not depend on δ and equals the following expression

$$|r_s|^2 = \left| \frac{k_{\|1} + k_{\|2}}{k_{\|1} - k_{\|2}} \right|^2$$

where

$$k_{\|1} = \sqrt{(\Omega - 1 + \lambda)(\Omega - (1-\lambda)(1+\Omega_0^*))}$$

and

$$k_{\|2} = \sqrt{(\Omega - 1)(\Omega - 1 - \Omega_0^*)}\ .$$

Here $\mathrm{Im}\ k_{\|1,2} > 0$, when $\mathrm{Im}\ \Omega > 0$. The expression for $|r_s|^2$ has a singularity, when $\Omega = (2-\lambda)(1+\Omega_0^*)/(2+\Omega_0^*)$, while any smooth profile has $\max |r_t|^2 \leq 2$. To avoid this singularity in the plot we take $\Omega = \mathrm{Re}\ \Omega + 0.02\,i$. A comparison of Fig. 12 and Fig. 13 qualitatively explains why the steep profile is significantly more unstable than the smooth profile for large δ.

One can readily show that instability corresponds to real Ω values where $|r_w r_t| > 0$. Using Eqs. (A6) and (A14), one can show there are two unstable regions for κ. The first is for small κ,

$$\kappa \leq \frac{\sqrt{(\Omega_r - \Omega_1)(\Omega_r - \Omega_2)}}{\Omega_r} \frac{\sqrt{1+q} - 1}{\sqrt{1+q} + 1}\ , \tag{A18}$$

where $\Omega_r \equiv \mathrm{Re}\,\Omega$, $\Omega_1 = 1 - \lambda$, $\Omega_2 = (1 + \Omega_0^*)(1 - \lambda)$, and the second is for large κ,

$$\kappa \geq \frac{\sqrt{(\Omega_r - \Omega_1)(\Omega_r - \Omega_2)}}{\Omega_r} \frac{\sqrt{1+q} + 1}{\sqrt{1+q} - 1}\ , \tag{A19}$$

For example, without FLR effects, i.e. if $\Omega^* = 0$, the stable range is

$$(1 - \Omega_1/\Omega_r)\frac{\sqrt{2} - 1}{\sqrt{2} + 1} < \kappa < (1 - \Omega_1/\Omega_r)\frac{\sqrt{2} + 1}{\sqrt{2} - 1}\ , \tag{A20}$$

On the other hand, we have FLR stabilization, when $\Omega_2 \geq 1$, because the condition that there be a finite tunneling region, given by Eq. (A7), does not exist. In terms of Ω_0^*, the stability condition is

$$\Omega_0^* > \frac{1}{1-\lambda} - 1 \ . \tag{A21}$$

Of course, our calculations are valid only if the first turning point lies sufficiently far from the end-wall, in order for the WKB approximation to be valid. It means, that

$$\kappa_{\|w}^2 \gg \frac{\partial \kappa_{\|}}{\partial x}$$

or

$$(\Omega_r - \Omega_2)^3 (\Omega_r - \Omega_1) \gg \frac{1}{\delta^2} \ . \tag{A22}$$

More detailed analysis for solving the eigenvalue problem should also take into account the wave phases. When both factors on the left side of Eq. (A22) are small compared with unity, but δ is large enough to validate this inequality, this phase information is accounted for in the method of solution described below. However for the most unstable solutions we need to obtain numerical solutions.

To proceed with the alternate method, we note that for large enough δ we can expand $\Omega_E(x)$ and $\Omega^*(x)$, as

$$\Omega_E(x) = \Omega_E(0) + x \frac{d\Omega_E(x=0)}{dx} \ ; \quad \Omega^*(x) = \Omega^*(0) + x \frac{d\Omega^*(x=0)}{dx} \ .$$

In terms of our standard profile, we have

$$\Omega_E(0) = 1 - \lambda \ , \quad \frac{\partial \Omega_E(0)}{\partial x} = \lambda \ , \quad \Omega^*(0) = (1-\lambda)\Omega_0^* \ ,$$

$$\frac{\partial \Omega_i^*(x=0)}{\partial x} = \lambda \Omega_0^* \ .$$

Equation (6) then becomes

$$\frac{d^2\xi}{dx^2} + \delta^2 (\Omega - 1 + \lambda - \lambda x) \left[\Omega - (1 - \lambda + \lambda x)(1 + \Omega_0^*) \right] \xi = 0 \ . \tag{A23}$$

The equation is accurate for $x < 1$. For sufficiently large x, this solution will have an outgoing wave solution that is spatially damped when $\mathrm{Im}\,\Omega > 0$, that is of the form,

$$\xi \propto \exp\left(-i\delta \int_0^x dx'\, q(x')\right)$$

where $q(x) = (\Omega + \lambda - 1 - \lambda x)^{1/2}\left[\Omega - (1+\Omega_0^*)(1-\lambda+\lambda x)\right]^{1/2}$, with $\dfrac{\partial q(x,\Omega)}{\partial \Omega} > 0$ for sufficiently positive x (and Ω nearly real). By using WKB techniques, this solution can be shown to match the correct boundary conditions at large x when $\delta \gg 1$.

Equation (A23) can be reduced to the standard form for cylindrical functions

$$\frac{d^2\xi}{dz^2} + \left[(\nu + 1/2) - \frac{z^2}{4}\right]\xi = 0$$

where

$$\nu = -\frac{1}{2} + \frac{i\delta\,\Omega^2\,\Omega_0^{*^2}}{8\lambda(1+\Omega_0^*)^{3/2}} \equiv -\frac{1}{2} + i\alpha$$

$$z \equiv |z|e^{i\theta} = z_0 + x e^{i\pi/4}(2\delta\lambda)^{1/2}(1+\Omega_0^*)^{1/4}$$

$$z_0 = \left(\frac{\delta}{2\lambda}\right)^{1/2} \frac{e^{-3i\pi/4}[\Omega(2+\Omega_0^*) - 2(1-\lambda)(1+\Omega_0^*)]}{(1+\Omega_0^*)^{3/4}} \equiv p_0\, e^{-3i\pi/4}\,. \tag{A24}$$

Note that the parameters α and p_0 are defined in Eq. (A24).

The solution that is well behaved for $|z| \to \infty$ and $\theta \simeq 0$ is the one that corresponds to outgoing group velocity for $\theta \sim \pi/4$. At $z = z_0$ we have

$$\frac{1}{\xi(z_0)}\frac{d\xi(z_0)}{dz} \equiv \left(\frac{\delta}{2\lambda}\right)^{1/2} \frac{\Omega\kappa\, e^{-3i\pi/4}}{(1+\Omega_0^*)^{1/4}} \equiv \eta\, e^{-3i\pi/4}$$

which implicitly defines η.

The solution for $\xi(z)$ is $\xi(z) = D_\nu(z)$, where D_ν denotes the cylindrical function.[16] Thus the dispersion relation is

$$\frac{D_\nu'(z_0)}{D_\nu(z_0)} = \eta\, e^{-3i\pi/4}\,. \tag{A25}$$

To proceed further, we assume $|z_0| \gg \max(1, |\nu|^{1/2})$, and we can then use the asymptotic expansion[16] for $D_\nu(z)$ near $z = |z_0|e^{-3i\pi/4}$. We thus have for $p = z\exp(3i\pi/4)$

$$e^{-3i\pi/8}\, D_\nu(pe^{-3i\pi/4}) \approx \frac{\exp(\alpha 3\pi/4)}{p^{1/2}}\left[\exp(-i\Phi(p)) + r\exp(i\Phi(p))\right] \tag{A26}$$

with $\Phi(p) \simeq \dfrac{p^2}{4} - \alpha \ln p$ and

$$r = \frac{-i(2\pi)^{1/2}\exp(-\pi\alpha/2)}{\Gamma\left(\dfrac{1}{2} - i\alpha\right)} \equiv |r|e^{i(\psi-\pi/2)} \ . \tag{A27}$$

For real α the magnitude of r is given by

$$|r| = \frac{(2\pi)^{1/2}\exp(-\pi\alpha/2)}{\left|\Gamma\left(\dfrac{1}{2} - i\alpha\right)\Gamma\left(\dfrac{1}{2} + i\alpha\right)\right|^{1/2}} = (1 + \exp(-2\pi\alpha))^{1/2} \ . \tag{A28}$$

If we match this exact result to Stirling's approximation for large α and the $\alpha = 0$ result, we can write an interpolation formula for r given by

$$r \simeq (1 + \exp(-2\pi\alpha))^{1/2}\exp\left[i\alpha(\ln\,\alpha - 1) - i\pi/2\right] \ .$$

This result is asymptotic for $|\alpha| \gg 1$ and exact for $\alpha = 0$. Now if we use Eqs. (A27) and (A28) with $\Phi(p) \approx \dfrac{p_0^2}{4} - \alpha\,\ln\,p_0$, we find

$$\frac{1 - \left(1 + \exp(-2\pi\alpha)\right)^{1/2}\exp\left(2i\Phi(p_0) + i\psi_\alpha\right)}{1 + \left(1 + \exp(-2\pi\alpha)\right)^{1/2}\exp\left(2i\Phi(p_0) + i\psi_\alpha\right)} = -\frac{2\eta}{p_0} \equiv -\tilde{\eta} \tag{A29}$$

with $\psi_\alpha = \alpha(\ln\,\alpha - 1) - \pi/2$. We can rewrite Eq. (A29) as

$$\exp\left(2i\Phi(p_0) + i\psi_\alpha\right) = \frac{1 + \tilde{\eta}}{1 - \tilde{\eta}}\,\frac{1}{[1 + \exp(-2\pi\alpha))]^{1/2}} \tag{A30}$$

or

$$2\Phi(p_0) + \psi_\alpha + \frac{\pi}{2} = 2(m \pm 1/2)\pi - i\ln\left|\frac{1 + \tilde{\eta}}{1 - \tilde{\eta}}\,\frac{1}{[(1 + \exp(-2\pi\alpha)]^{1/2}}\right| \tag{A31}$$

where m is a positive integer and the $+$ sign is for $\tilde{\eta} < 1$ and $-$ sign for $\tilde{\eta} > 1$. We then find

$$\left[\Omega(2+\Omega_0^*) - 2(1-\lambda)(1+\Omega_0^*)\right]^2 - \Omega^2\Omega_0^{*2}\left\{\ln\left[\frac{2[\Omega(2+\Omega_0^*) - 2(1-\lambda)(1+\Omega_0^*)]}{\Omega\Omega_0^*}\right] + \frac{1}{2}\right\}$$

$$= \frac{4}{\delta}\left[2(m \pm 1/2)\pi - i\ln\left|\frac{1+\tilde{\eta}}{(1-\tilde{\eta})\left[1+\exp(-2\pi\alpha)\right]^{1/2}}\right|\right]\lambda(1+\Omega_0^*)^{3/2}\,. \qquad \text{(A32)}$$

In the limit $\delta \to \infty$ and $\Omega_0^* \neq 0$ Eq. (A32) only gives stable roots. For δ finite there can be instability regions. The stable regions are where the argument of the logarithm is less than unity. From this condition the stability band satisfies

$$\frac{\left[1+\exp(-2\pi\alpha)\right]^{1/2}+1}{\left[1+\exp(-2\pi\alpha)\right]^{1/2}-1} > \tilde{\eta} > \frac{\left[1+\exp(-2\pi\alpha)\right]^{1/2}-1}{\left[1+\exp(-2\pi\alpha)\right]^{1/2}+1} \qquad \text{(A33)}$$

where we recall that

$$\alpha = \delta\Omega^2\Omega_0^{*2}/8\lambda\left(1+\Omega_0^*\right)^{3/2}$$

and

$$\tilde{\eta} = \Omega\kappa(1+\Omega_0^*)^{1/2}/\left[\Omega(1+\Omega_0^*/2) - (1-\lambda)(1+\Omega_0^*)\right]$$

and we take Ω as real. One can readily find consistency between the instability conditions given by Eqs. (A18) and (A19) and the stability condition given by Eq. (A33) (taking into account that, for validity of our expansion in Eq. (A23), we need $\Omega_0^* \ll 1$ and $\mathrm{Re}\,\Omega - 1 + \lambda \ll 1$). In the case $\Omega^* = 0$ coincidence becomes exact, because the reflection coefficient from the tunneling region is $|r_t|^2 = |r|^2 = 2$ in both models while the end-wall reflection coefficient does not depend on the profile shape.

The analytic results can be compared with thresholds obtained numerically. For $\Omega_0^* = 0$ and $\lambda = 0.7$, we have that $\tilde{\eta} = \Omega\kappa/[\Omega - 1 + \lambda]$. In Fig. 5b we plot curves that are unstable at small δ, and stabilize at a critical δ value. The larger the δ value the better correlation we would expect with our asymptotic analysis. For $\kappa < .14$, marginal stability occurs at δ values that are larger than the range plotted. The threshold condition for some of these values (see Fig. 14) are: $\kappa = 0.08$, $\delta \simeq 22$, $\mathrm{Re}\,\Omega \simeq 0.48$; $\kappa = 0.10$, $\delta \simeq 11$, $\mathrm{Re}\,\Omega \simeq 0.55$; $\kappa = .12$,

$\delta \simeq 5.4$, Re $\Omega \simeq 0.63$. For all these values we find that by substituting the numerical values into the expression for $\tilde{\eta}$ (just after Eq. (A33)), we find $\tilde{\eta} \simeq 0.21, .22, .23$, respectively, which shows an insensitivity to the value of κ. This result should be compared to the asymptotic threshold prediction (when $(\alpha = 0)$ $\tilde{\eta} = (\sqrt{2}-1)/\sqrt{2}+1 \simeq 0.172$. The absolute magnitude of the predictions differ by $\sim 25\%$. This discrepancy probably arises because the asymptotic analysis requires z_0 in Eq. (A24) to be large, whereas numerically we find for these solutions that $z_0 \approx 1$. A similar correlation arises when applying Eq. (A18) at marginal stability [i.e., when κ is set equal to the right-hand side of (A18)]. For $\Omega_0^* = 0$ and $\lambda = 0.7$, and taking $\mathrm{Re}\,\Omega = 0.48$, we find that Eq. (A18) predicts $\kappa = 0.064$; $\mathrm{Re}\,\Omega = 0.55$ implies $\kappa = 0.078$, while $\mathrm{Re}\,\Omega = 0.63$ implies $\kappa = 0.091$, which should be compared with the numerically obtained values of κ quoted above.

Somewhat better correlation is found with the numerical results in Fig. 7, which shows instability arising as κ increases. In Table I a list of selected threshold values obtained numerically is shown. By using the numerical values of δ $\mathrm{Re}\,\Omega$, and $\Omega_0^* = 0.1$, and equating $\tilde{\eta}$ to the left-sided expression in the inequality listed in Eq. (A33), we infer a value of κ, which we call κ_1. We see in the table that the numerical value of κ and κ_1 agree within 10%. In this case $z_0 \simeq 3$, which better justifies the asymptotic analysis than in the first case. Similarly, by using Eq. (A19) at equality, and the numerical values of Ω and δ listed in Table I, we obtain a prediction for κ which is called κ_2. As expected, κ_2 is more accurate than κ_1.

If m is large we can solve for Ω_0 analytically as well. Though this approximation is too crude to compare with our numerical results, it does give us some insight into stability conditions for other modes. For $\Omega_0^* = 0$, the dispersion relation is

$$(\Omega + \lambda - 1) = \left(\frac{\lambda}{\delta}\right)^{1/2} \left[2(m \pm 1/2)\pi + i\,\ell n \left|\frac{(1-\tilde{\eta})\sqrt{2}}{(1+\tilde{\eta})}\right|\right]^{1/2}. \tag{A34}$$

At marginal stability for the case $\tilde{\eta} < 1$, we find

$$\Omega_0 = 1 - \lambda + \left(\frac{\lambda\pi(m - 1/2)}{\delta}\right)^{1/2} \qquad \tilde{\eta} = \kappa\left[\frac{(1-\lambda)\delta^{1/2}}{(\pi\lambda(2m-1))^{1/2}} + 1\right] .$$

For $\tilde{\eta} > 1$, we find

$$\Omega_0 = 1 - \lambda + \left(\frac{\lambda\pi(m + 1/2)}{\delta}\right)^{1/2} \qquad \tilde{\eta} = \kappa\left[\frac{(1-\lambda)\delta^{1/2}}{(\pi\lambda(2m+1))^{1/2}} + 1\right] . \tag{A35}$$

Thus the stability bands arise in the intervals,

$$\frac{\sqrt{2}+1}{\sqrt{2}-1}\Big/\left[(1-\lambda)\left(\frac{\delta}{\pi\lambda(2m+1)}\right)^{1/2} + 1\right] > \kappa > \frac{\sqrt{2}-1}{\sqrt{2}+1}\Big/\left[\frac{(1-\lambda)\delta^{1/2}}{(\pi\lambda(2m-1))^{1/2}} + 1\right] . \tag{A36}$$

To study finite Ω_0^* we restrict ourselves to $\Omega_0^* \ll 1$. From Eq. (A32) we then find

$$\Omega_0^{\pm} \doteq (1-\lambda)\left(1 + \frac{\Omega_0^*}{2}\right) + \left(\frac{2\pi(m \pm 1/2)\lambda}{\delta}\right)^{1/2} + \mathcal{O}\left(\Omega_0^{*2}\right) .$$

With these values of $\Omega_0^{\pm}$, we leave to the reader the exercise of substituting $\Omega_0^{\pm}$ in Eq. (A33) and finding an explicit stability band for κ. One readily observes that the stability bands become larger as Ω_0^* and δ increase.

References

[1]A.V. Nedospasov, Fiz. Plazmy **15**, 1139 (1989) [Sov. J. Plasma Phys. **15**, 659 (1989)].

[2]X. Garbet, L. Lauren, J.-P. Roubin and A. Samain, Nucl. Fusion **31**, 967 (1991).

[3]H.L. Berk, D.D. Ryutov, Yu.A. Tsidulko, JETP Lett. **52**, 674 (1990).

[4]H.L. Berk, D.D. Ryutov, Yu.A. Tsidulko, Phys. Fluids B **3**, 1346 (1991).

[5]H.L. Berk, R.C. Cohen, D.D. Ryutov, Yu.A. Tsidulko, and X.Q. Xu, Nucl. Fusion **33**, 263 (1993).

[6]B.B. Kadomtsev, in Proc. 7th Conf. on Phenomena in Ionized Gases, (Belgrade, 1965, Eds. B. Perovic and D. Tocsic) Grad Jevinska Kniga, Belgrade, Yugoslavia (1966), Vol. 2, p. 610.

[7]X.S. Lee, P.J. Catto, and R.E. Aamodt, Phys. Fluids **25**, 1491 (1982).

[8]H.L. Berk, M.N. Rosenbluth, H.V. Wong, T.M. Antonsen, and D.E. Baldwin, Fiz. Plasmy **9**, 176 (1983) [Sov. J. Plasma Phys. **9**, 108 (1983)].

[9]K.C. Shaing, G.S. Lee, B.A. Carreras, W.A. Houlberg, and E.J. Crume, Jr., in *Plasma Physics and Controlled Nuclear Fusion Research 1988*, Proc. 12th Int. Conf., Nice, France (IAEA, Vienna, 1989) Vol. 2, p. 13.

[10]Y.B. Kim, P.H. Diamond, H. Biglari, and P.W. Terry, Phys. Fluids B **2**, 2143 (1990).

[11]Asdex Team, Nucl. Fus. **29**, 1959 (1989).

[12]W. Kunkel, J. Guillory, in *Proc. 7th Conf. on Phenomena in Ionized Gases, 1965* Eds. B. Perovic and D. Tocsic (Grad Jevinska Kniga, Belgrade, Yugoslavia 1966), Vol. 2, p. 702.

[13]E.J. Doyle, *et al.*, Modifications in turbulence and edge electric fields at the L-H transition in DIII-D, General Atomics Project 3466, Jan. 1991.

[14]J. Heading, *An Introduction to Phase-Integral Methods*, London:Methuen, New York: John Wiley, 1962.

[15]H.J. Kull, R.J. Kashuba, and H.L. Berk, J. Math. Phys. **30**, 2527 (1989).

[16]H. Bateman and A. Erdelyi, *Higher Transcendental Functions*, Vol. 2, (New York, Toronto, London, McGraw-Hill, 1953).

Figure Captions

1. Real (a), and imaginary, (b), normalized frequencies for the sharp profile model as a function of δ, for $\lambda = 0.7$ and $\kappa = 0$. Various values of Ω_0^* are indicated on the curves. Note that Im $\Omega = 0$ for $\Omega_0^* = 2.33$.

2. Real (a), and imaginary, (b), normalized frequencies for the sharp profile model as a function of δ, for $\lambda = 0.7$ and $\kappa = 0.166$. Various values of Ω_0^* are indicated on the curves.

3. Imaginary normalized frequency for the sharp profile model as a function of δ, for $\lambda = 0.7$ and $\kappa = 0.414$ (a) and $\kappa = 0.58$ (b). Various values of Ω_0^* are indicated on the curves.

4. Example of two unstable modes present for a fixed δ in the sharp profile model. Here Im Ω vs. κ is plotted for $\delta = 10$, $\Omega_0^* = 0.5$ and $\lambda = .5$.

5. Real (a) and imaginary (b) normalized frequencies for smooth profile model as a function of δ, for $\lambda = 0.7$ and $\Omega_0^* = 0$. Various values of κ are indicated on the curves.

6. Real (a) and imaginary (b) normalized frequencies for smooth profile model as a function of δ, for $\lambda = 0.7$ and $\kappa = 0$. Various values of Ω_0^* are indicated in the curves.

7. Onset of instability with large κ values. The fixed parameters are $\Omega_0^* = 0.1$, $\lambda = 0.7$. The normalized imaginary frequency is shown as a function of κ for various values of δ.

8. Plot of the base 10 logarithm of Γ_m as a function of the base 10 logarithm of C_2 for various values of Ω_0^*.

9. Plot of D (curve 1) and L_T (curve 2) as a function of Ω_0^*.

10. Schematic plot of $E_1(x) = \Omega_E(x)$ and $E_2(x) = \Omega_E(x) + \Omega^*(x)$. Tunneling region is in the shaded area.

11. Plot of reflection coefficient $\ln |r_w|^2$ as a function of $\mathrm{Re}\,\Omega$ for sharp profile model. Here $\Omega_0^* = 0.5, \lambda = 0.7, \Omega_1 = 1 - \lambda$, $\Omega_2 = (1-\lambda)(1+\Omega_0^*)$ and $\Omega = \mathrm{Re}\,\Omega + .02i$. Figure (a) is for relatively small κ values, while Fig. (b) is for relatively large κ values.

12. Plot of $\ln |r_t|^2$ for smooth profile. Here $\lambda = 0.7, \Omega_0^* = 0.5, \Omega_1 = 1 - \lambda$, $\Omega_2 = (1 - \lambda)(1 + \Omega_0^*)$, $\Omega_3 = 1$ and $\Omega_4 = 1 + \Omega_0^*$. Results for various values of δ are indicated. Note $\ln |r_t|^2 = 0$ in the interval $\Omega_3 < \Omega < \Omega_4$ and $|r_t|^2$ is not defined for $\Omega < \Omega_2$ and $\Omega > \Omega_4$.

13. Plot of $\ln |r_s|^2$ for sharp profile. Here $\lambda = 0.7, \Omega_0^* = 0.5, \Omega_1 = 1 - \lambda$, $\Omega_2 = (1-\lambda)(1 + \Omega_0^*), \Omega_3 = 1$ and $\Omega_4 = 1 + \Omega_0^*$.

14. Imaginary normalized frequencies for smooth profile model as a function of δ, for $\lambda = 0.7$ and $\Omega_0^* = 0$. Various values of κ are indicated on the curves.

δ	Ω	κ	κ_1	κ_2
20	0.695	3.71	3.42	3.67
25	0.659	3.56	3.29	3.51
35	0.611	3.33	3.11	3.29
50	0.566	3.11	2.90	3.07

Table I.

Comparison of κ at instability threshold obtained numerically with κ_1 obtained from Eq. (A33) by using the left-sided relation at equality with the numerical values of Ω and δ (listed in table). Equation (A19) at equality, is used to predict the κ-value denoted as κ_2.

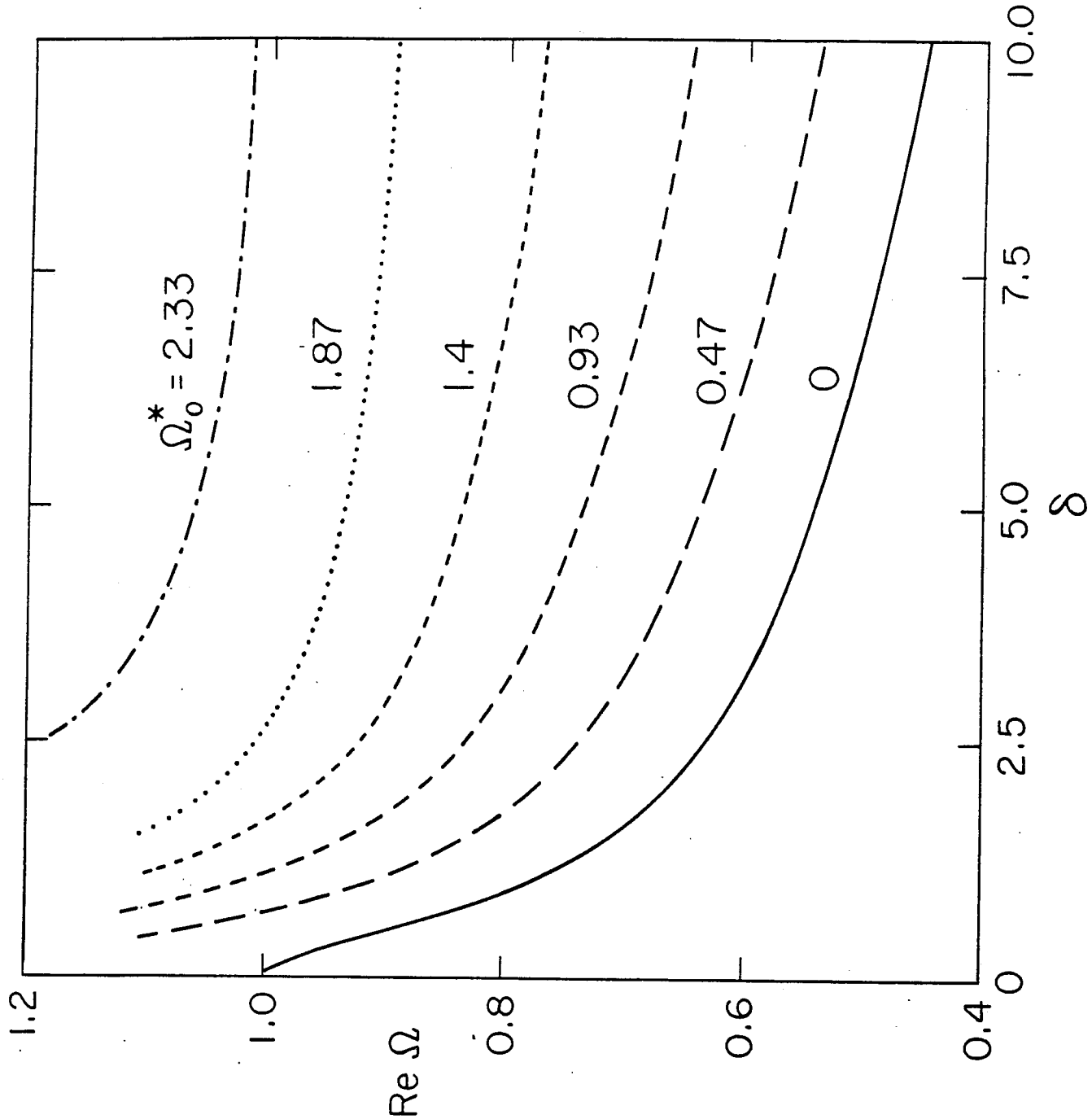

Fig. 1a

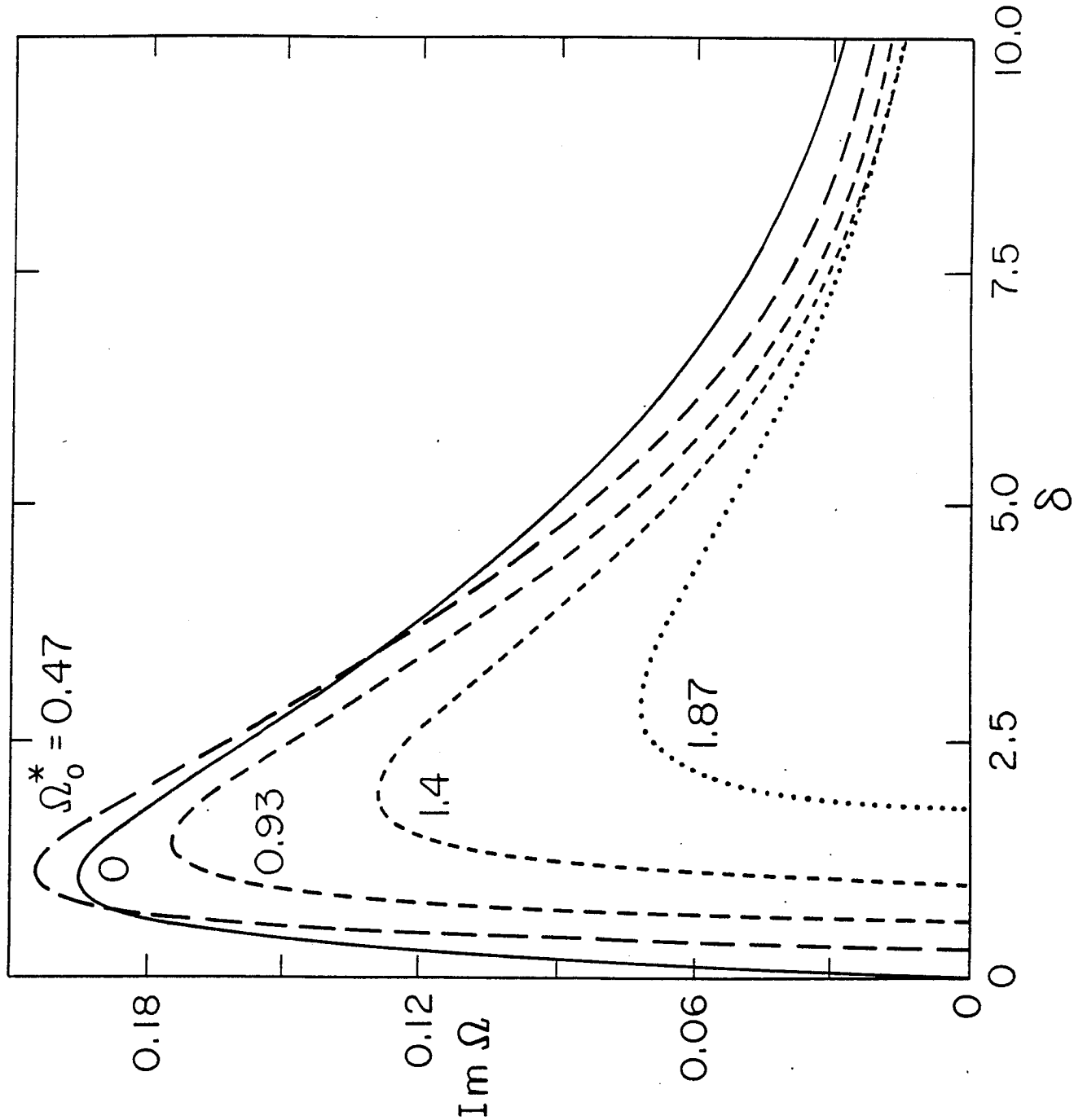

Fig. 1b

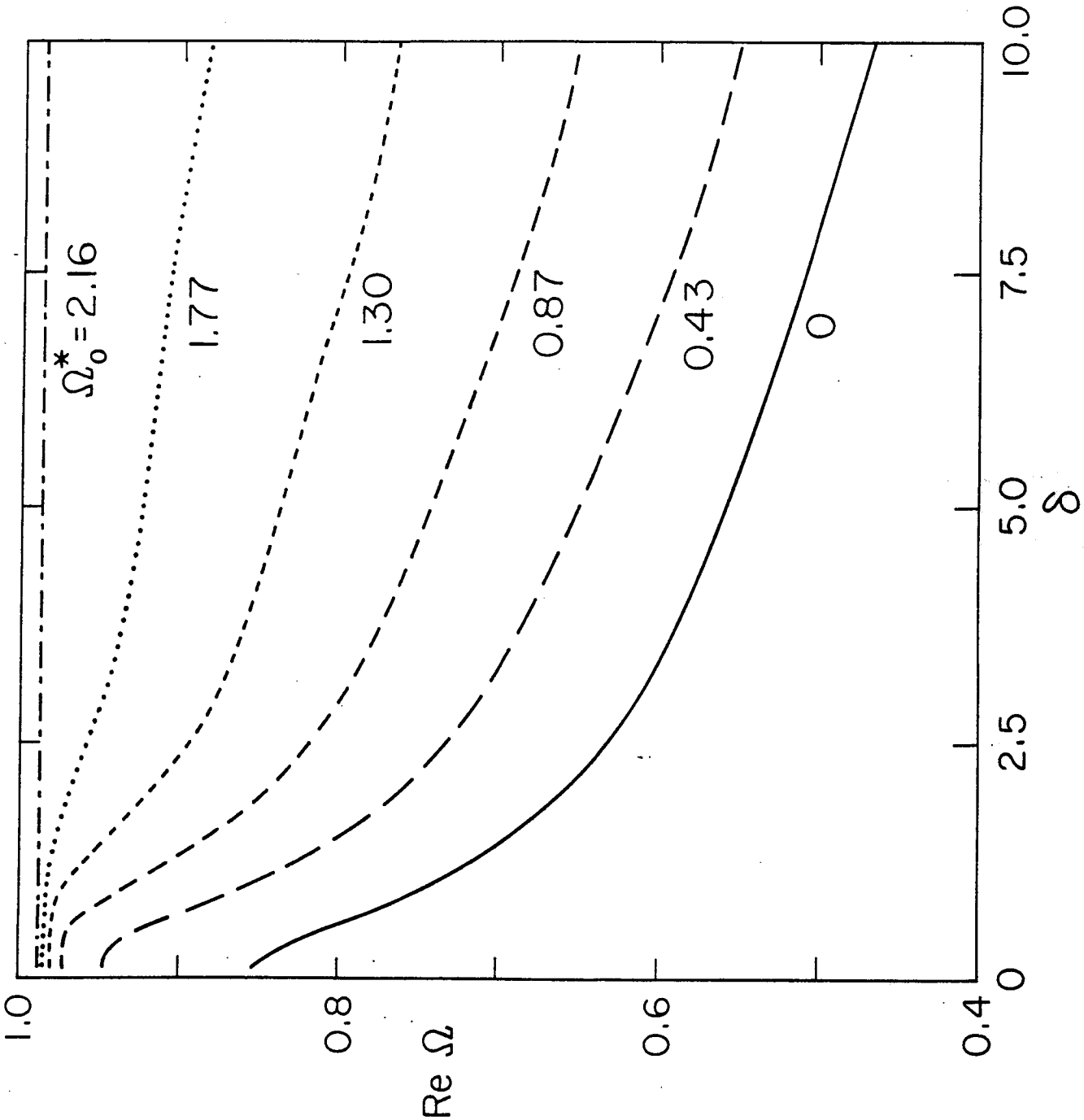

Fig. 2a

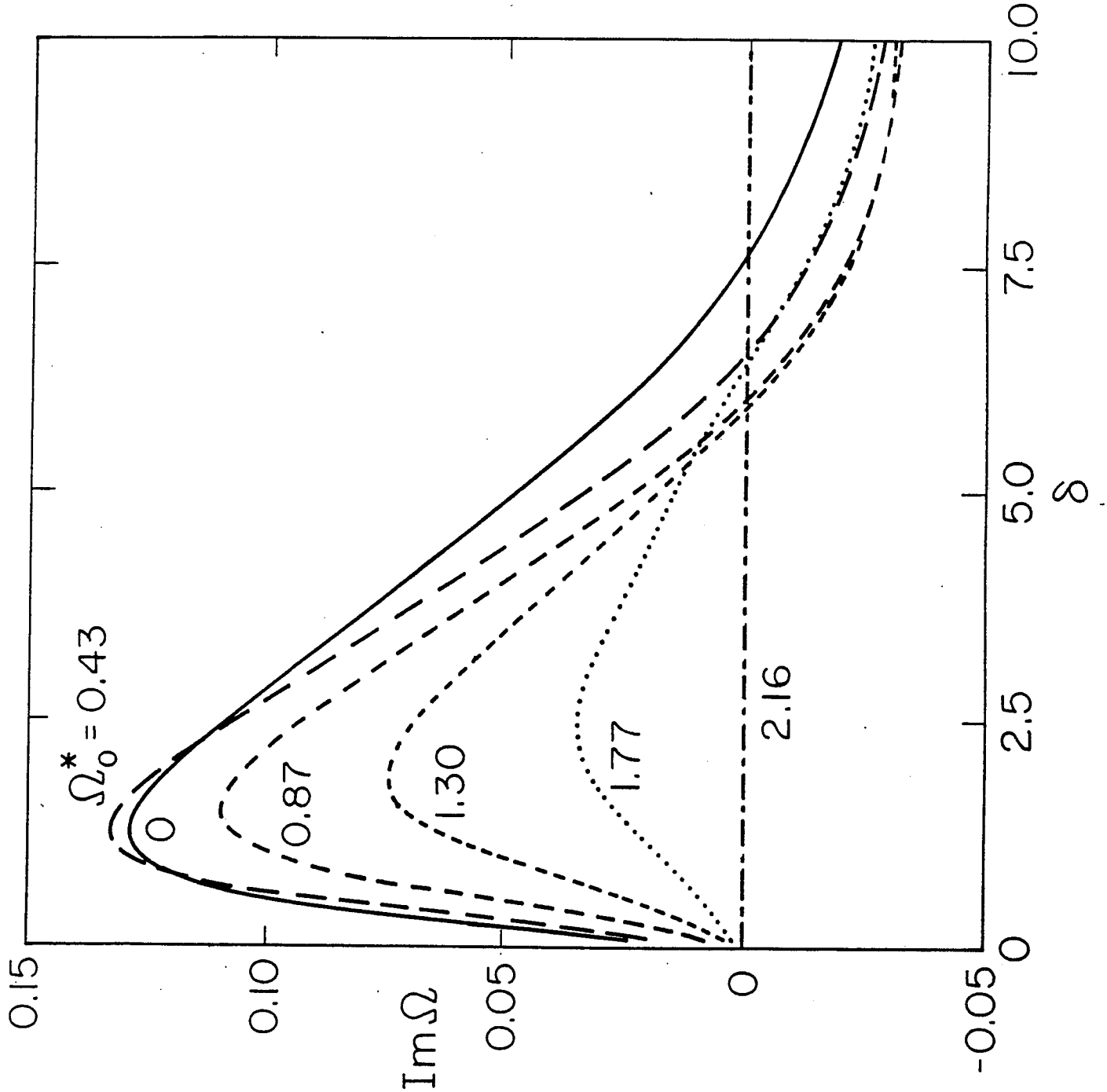

Fig. 2b

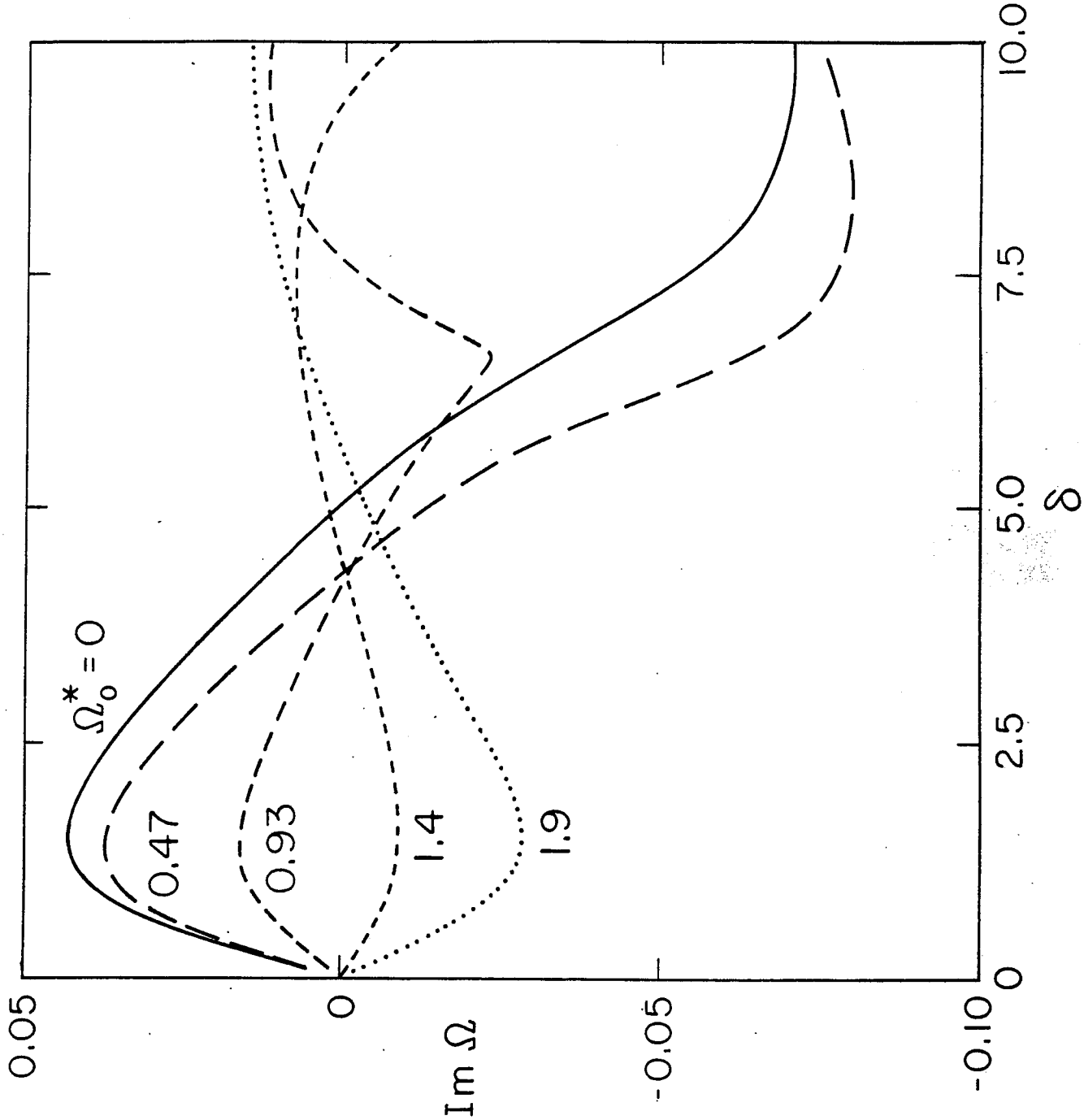

Fig. 3a

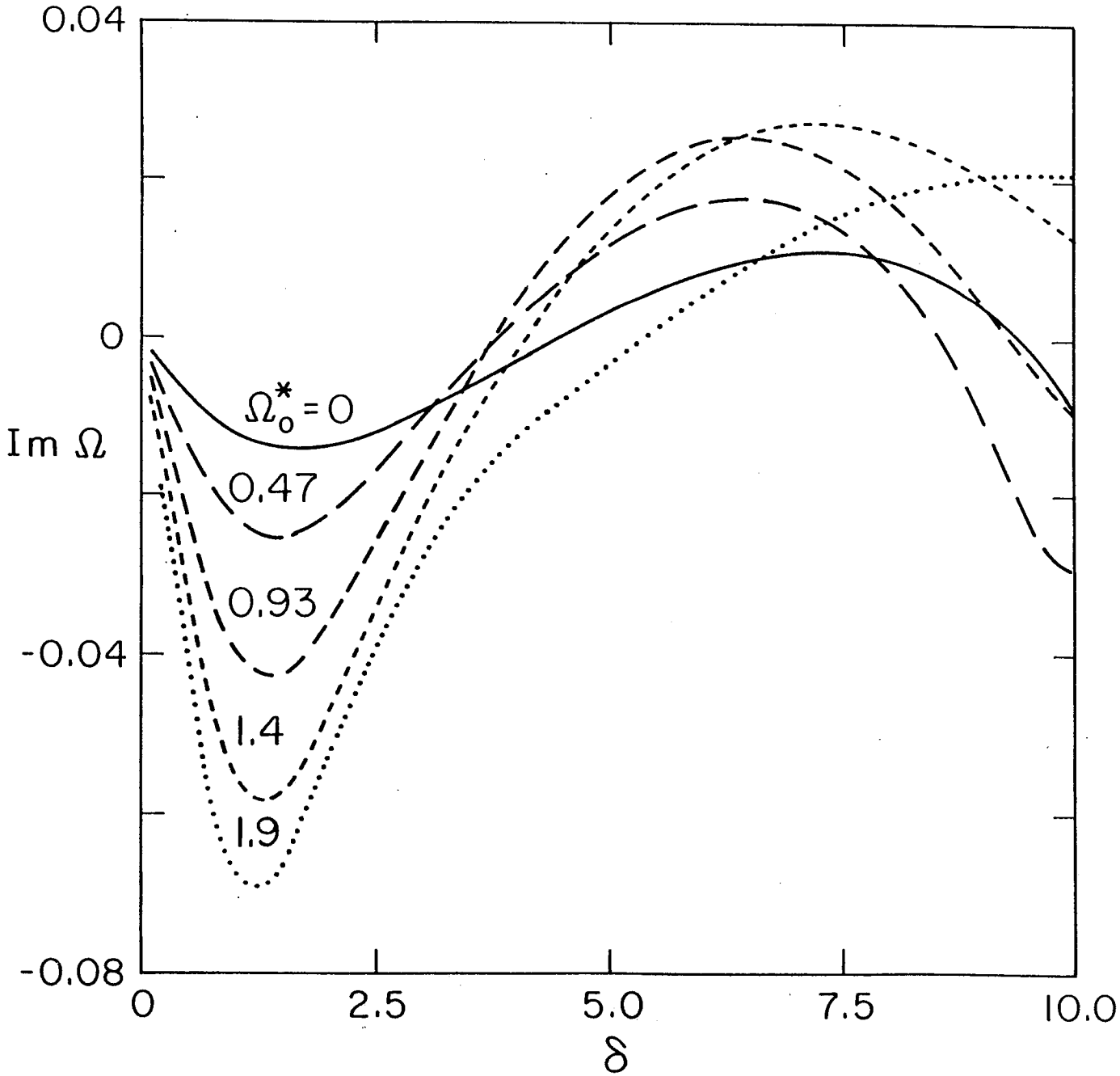

Fig. 3b

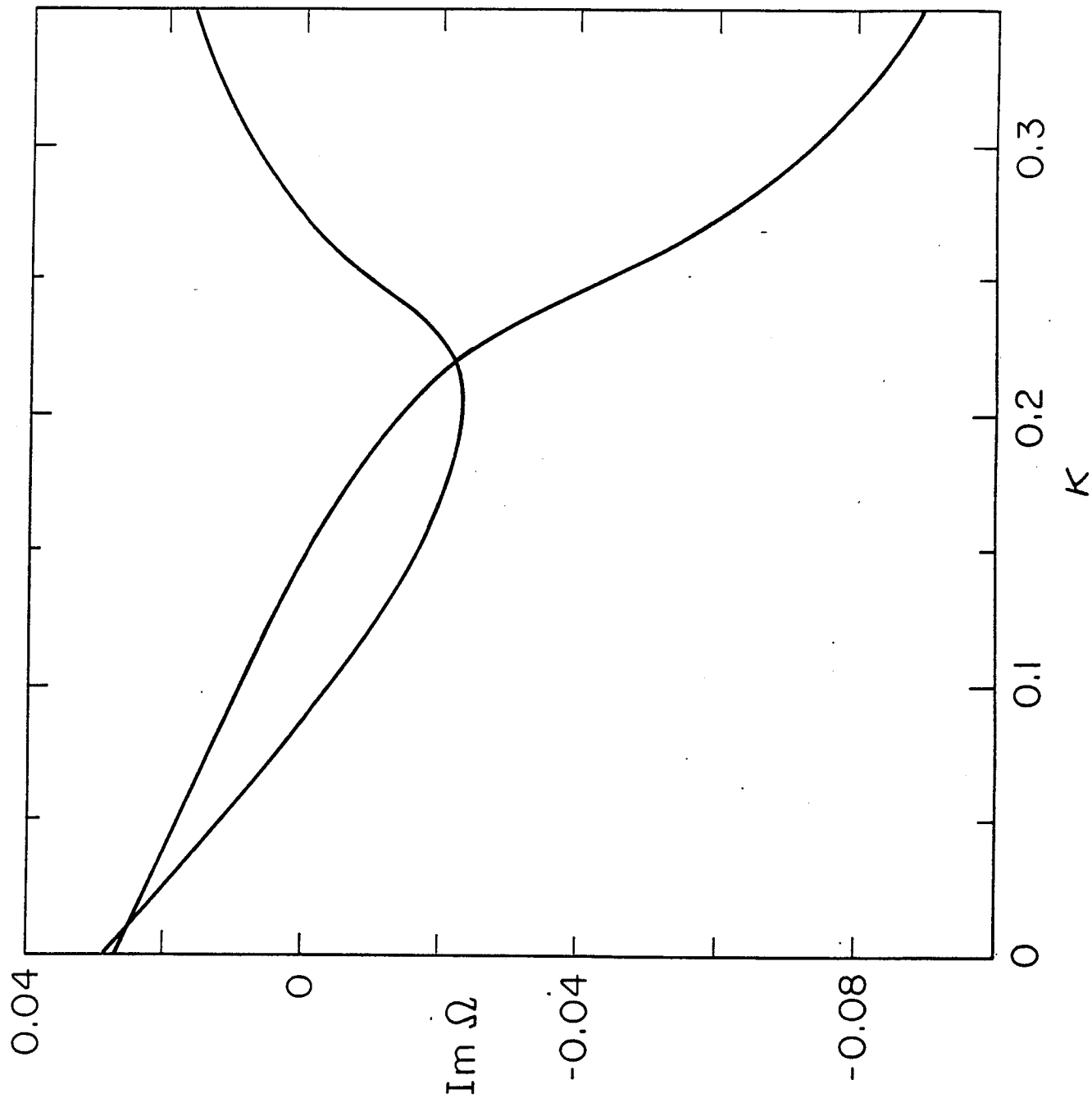

Fig. 4

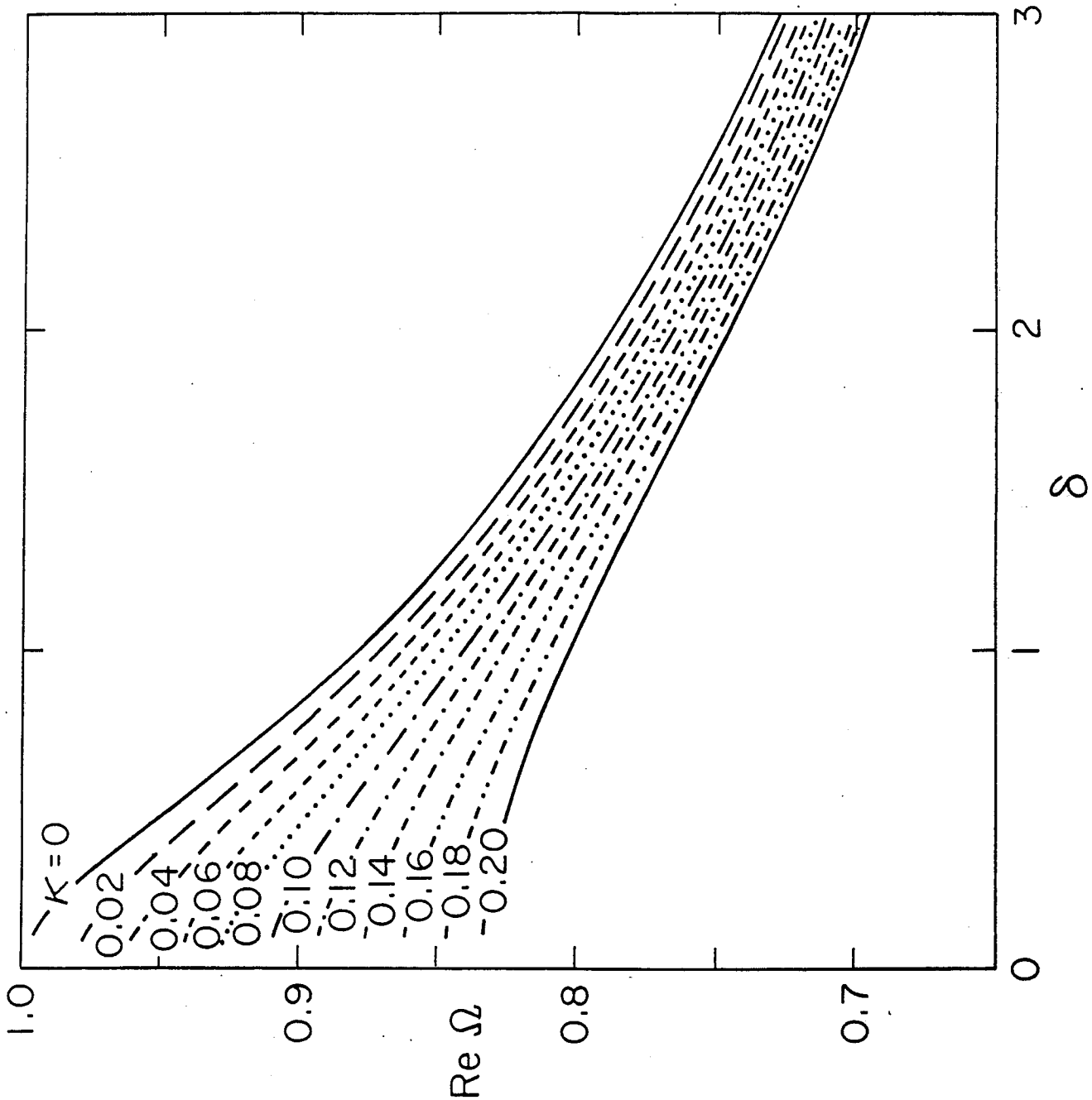

Fig. 5a

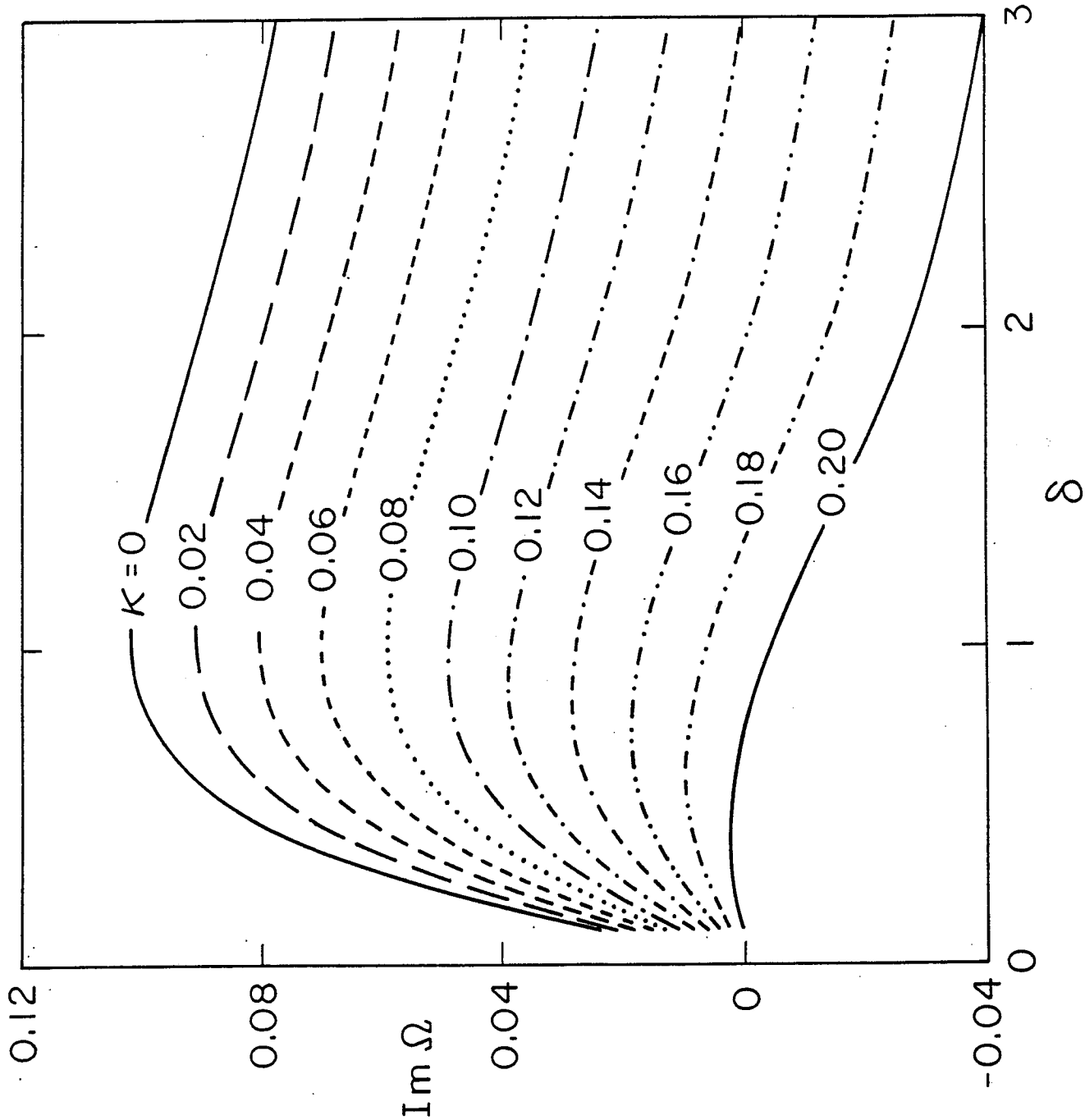
0.12
0.08
0.04
0
-0.04
Im Ω
0
1
2
3
δ
K = 0
0.02
0.04
0.06
0.08
0.10
0.12
0.14
0.16
0.18
0.20

Fig. 5b

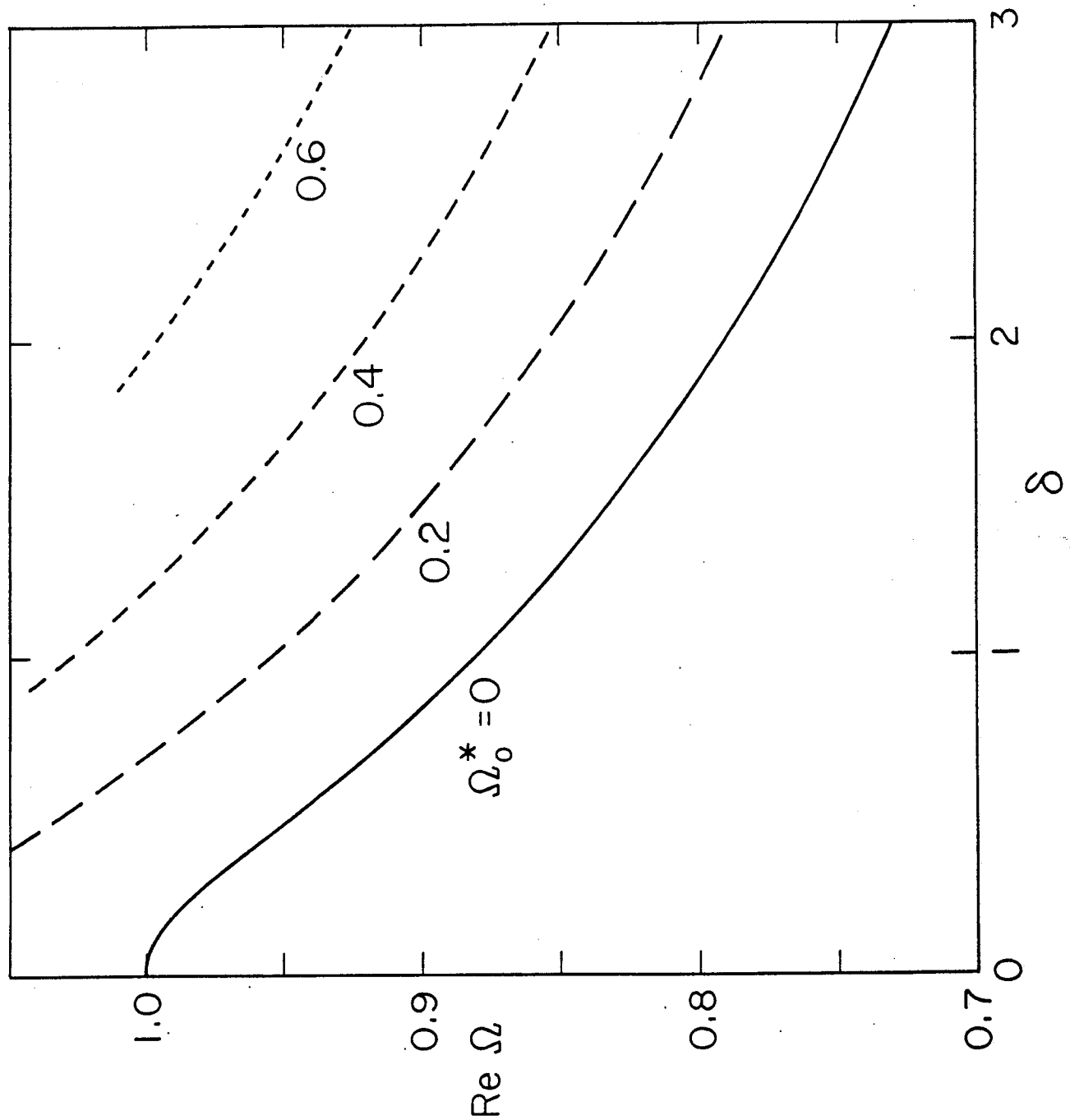

Fig. 6a

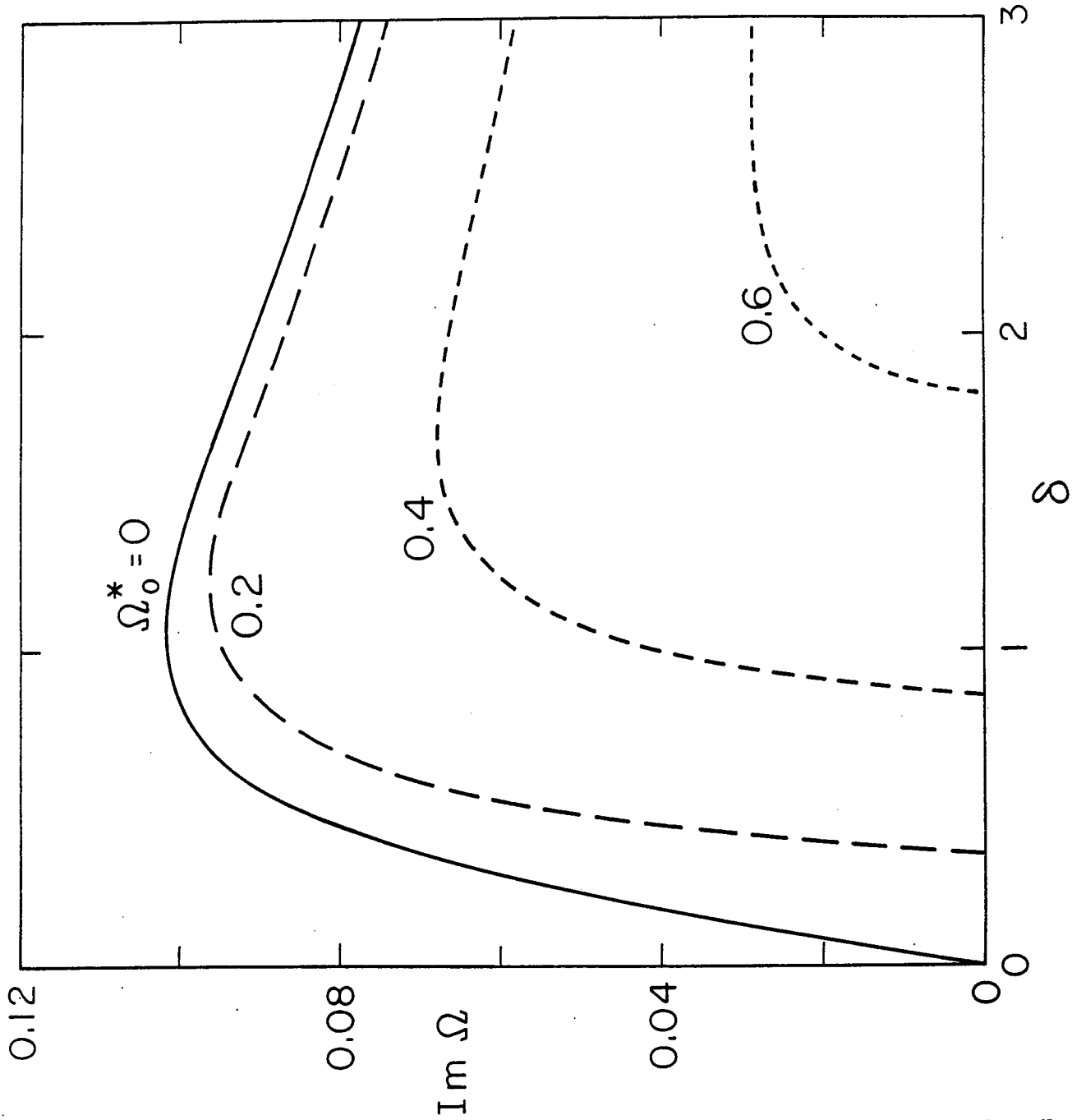

Fig. 6b

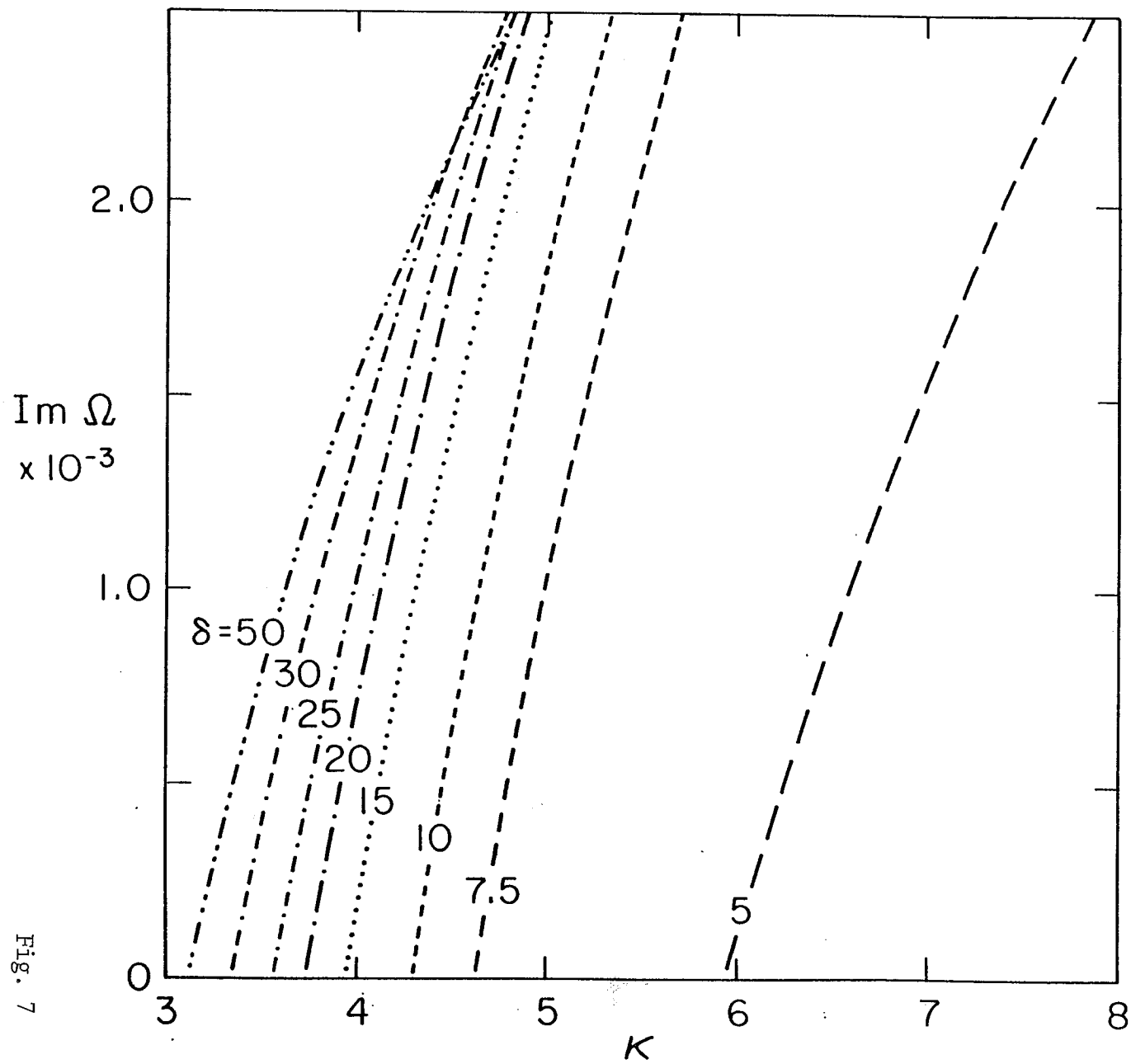

Fig. 7

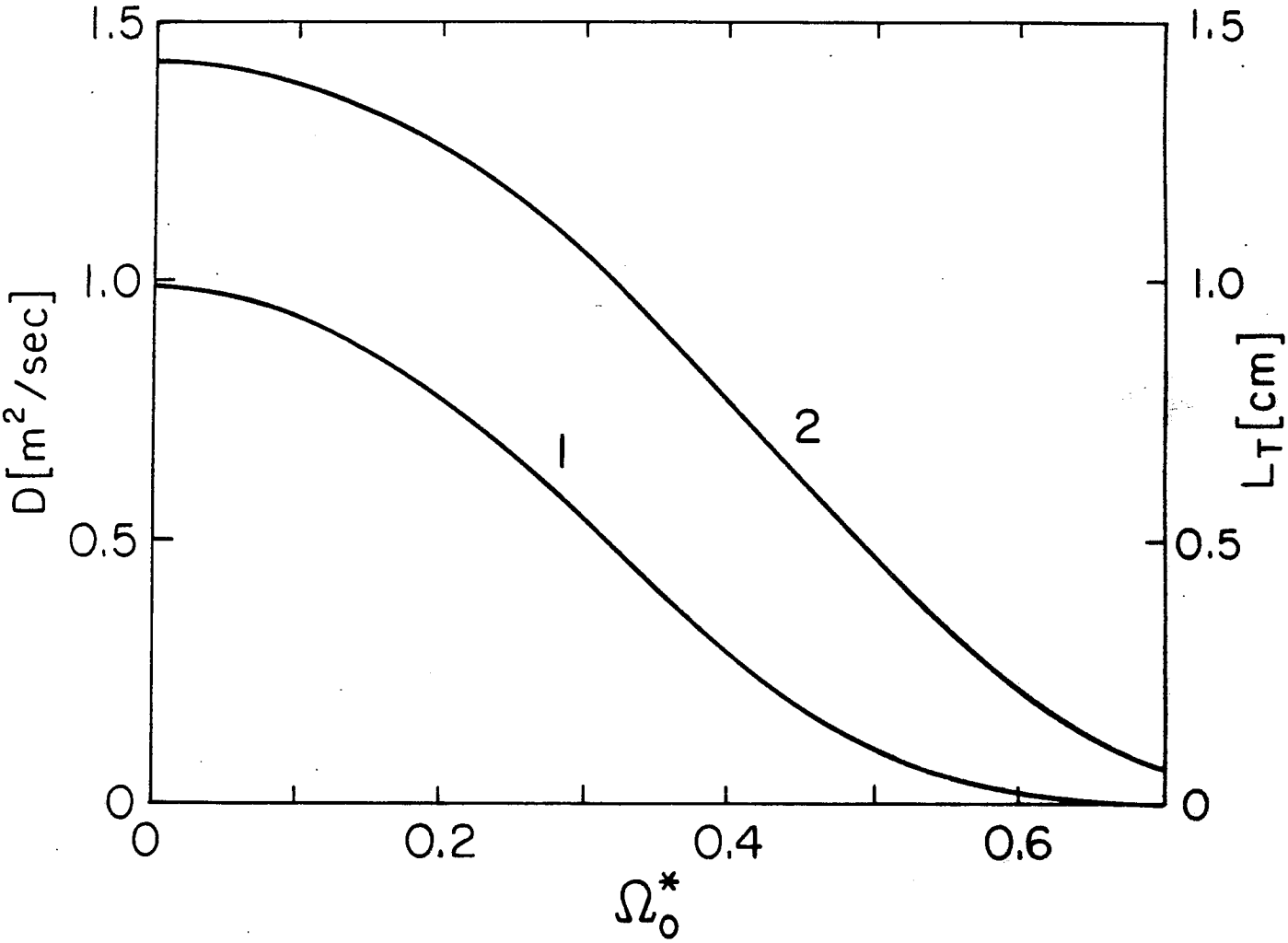

Fig. 8

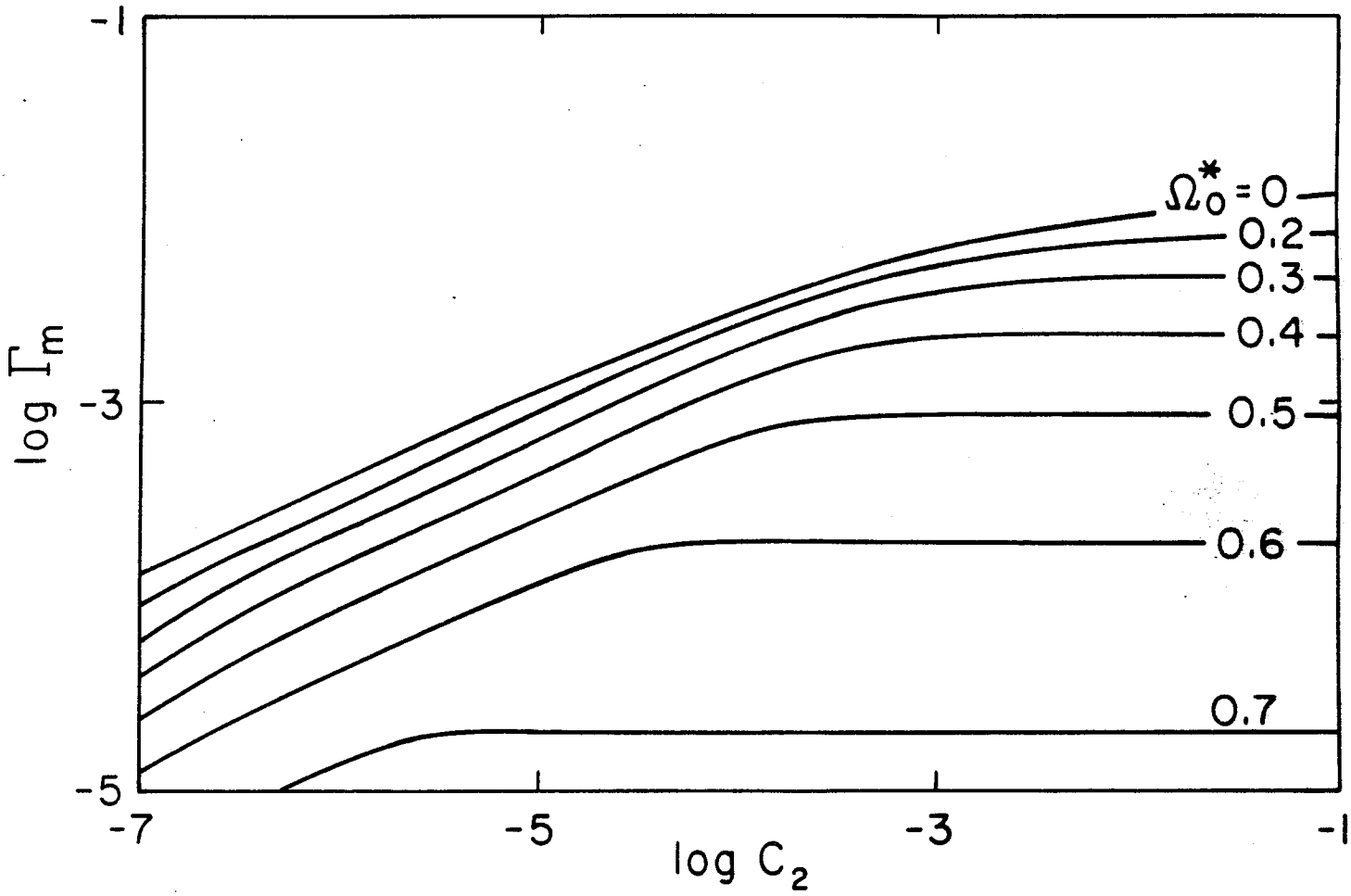

Fig. 9

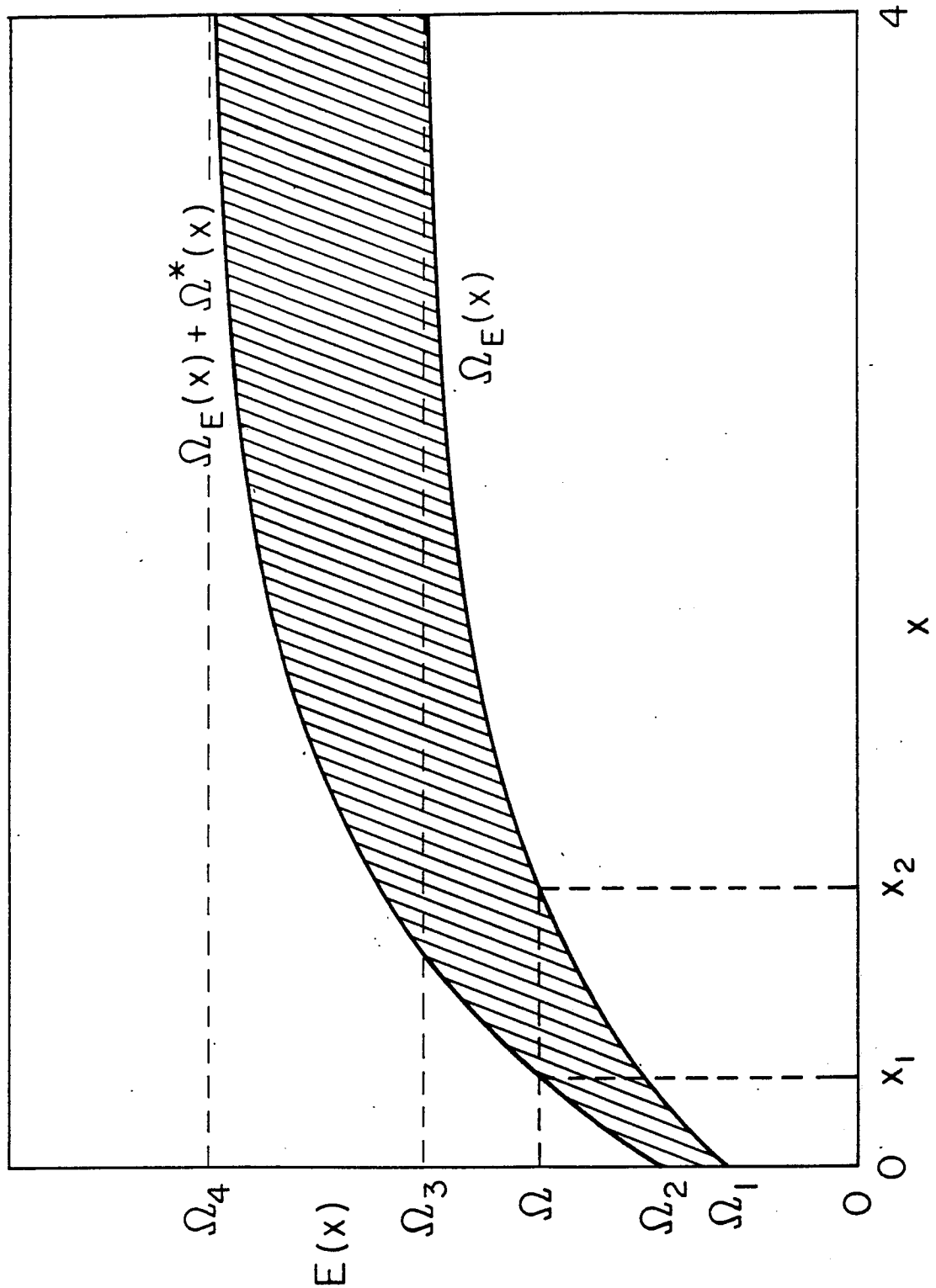
$\Omega_E(x) + \Omega^*(x)$
$\Omega_E(x)$
Ω_4
$E(x)$
Ω_3
Ω
Ω_2
Ω_1
0
0
x_1
x_2
x
4

Fig. 10

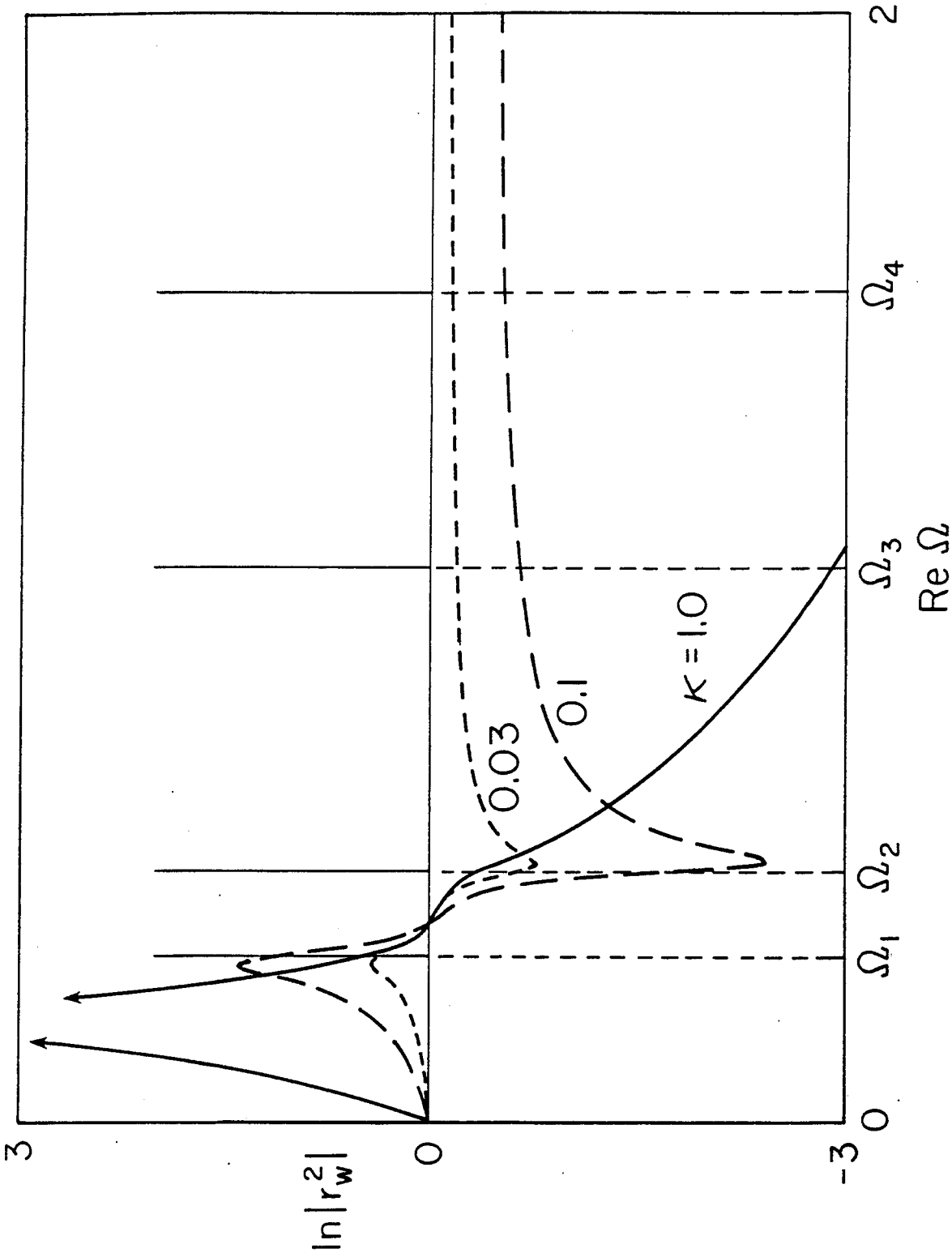
3
0
-3
$\ln|r_w^2|$
0
Ω_1
Ω_2
Ω_3
Ω_4
2
Re Ω
0.03
0.1
$\kappa = 1.0$

Fig. 11a

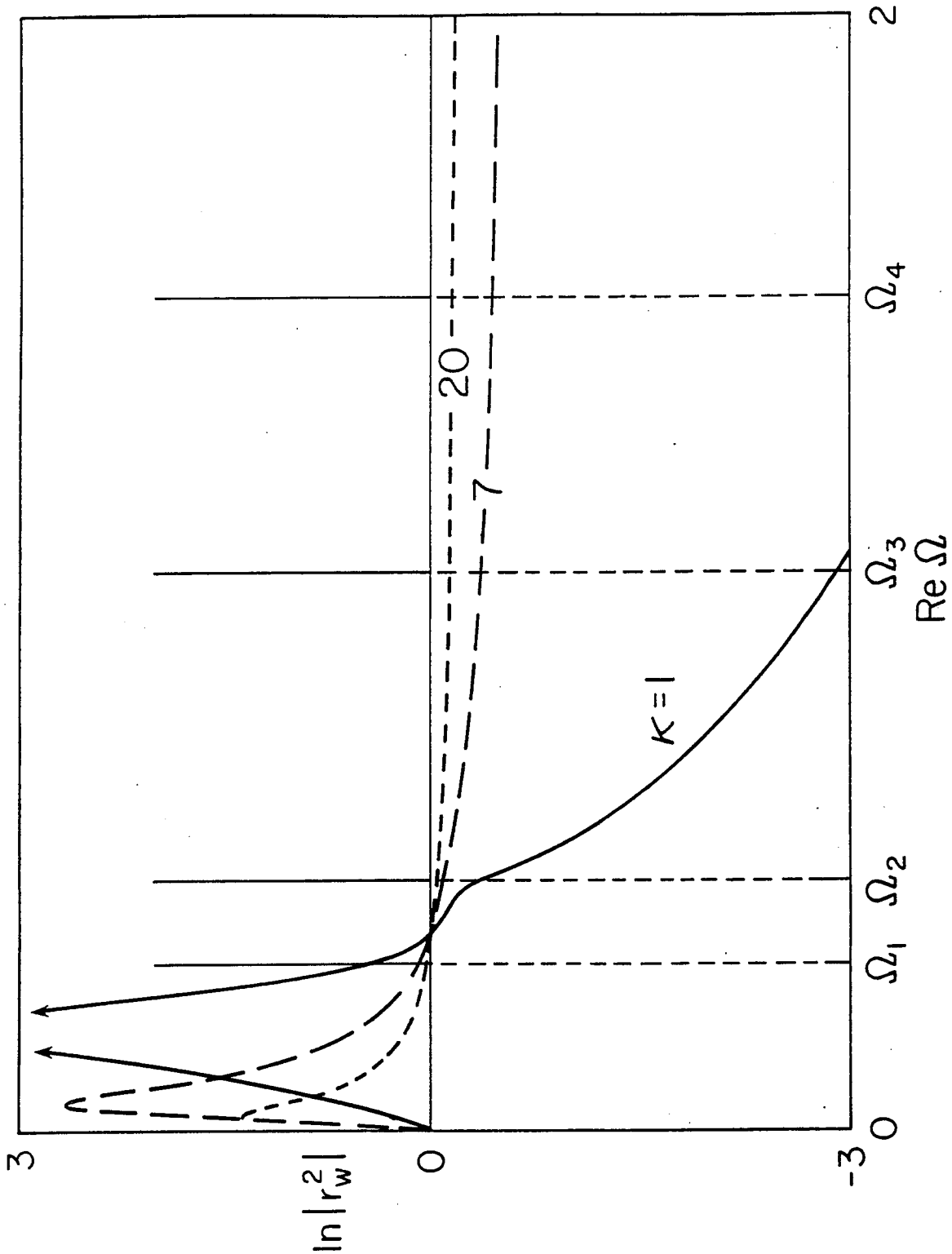
3
0
-3
$\ln|r_w^2|$
0
Ω_1
Ω_2
Ω_3
Ω_4
2
Re Ω
$\kappa=1$
20
7

Fig. 11b

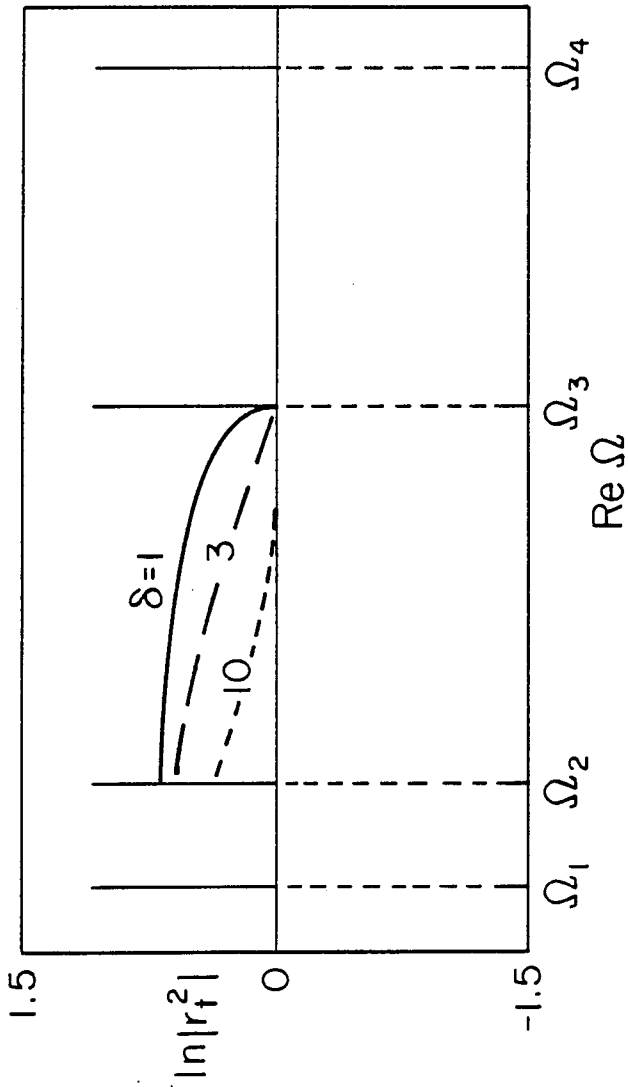
1.5
$\ln|r_t^2|$
0
-1.5
Ω_1
Ω_2
Ω_3
Ω_4
Re Ω
$\delta=1$
3
10

Fig. 12

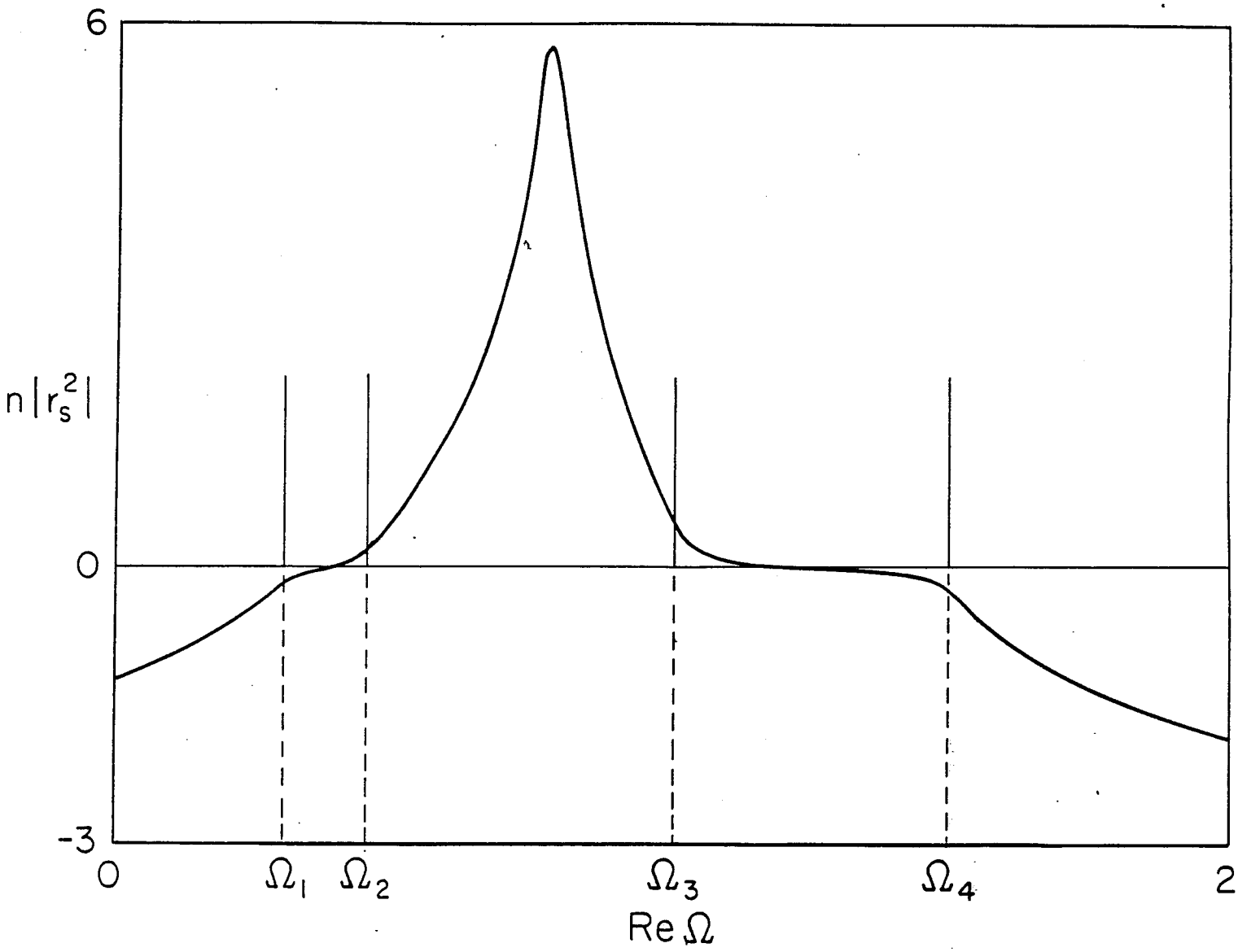

Fig. 13

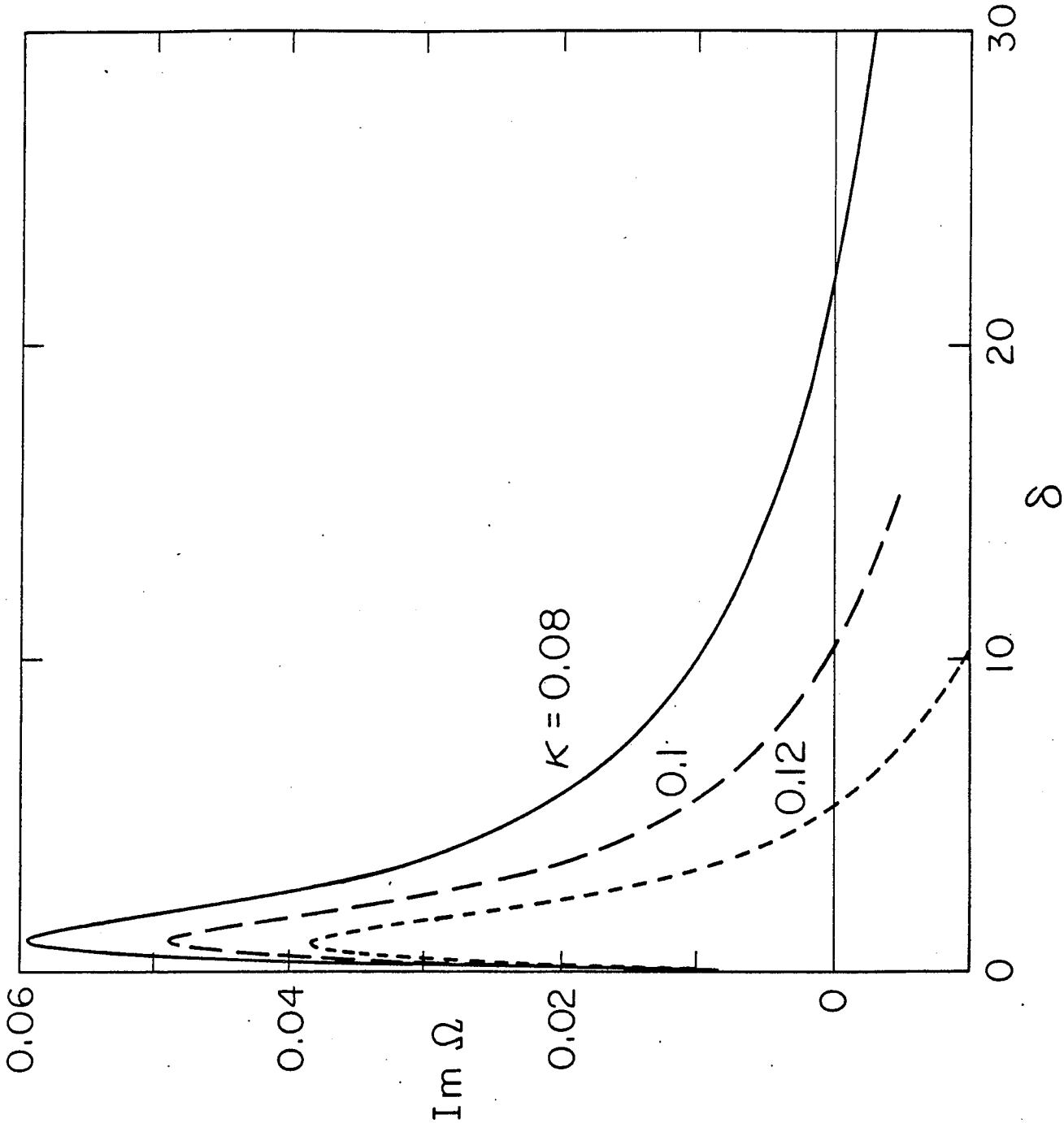

Fig. 14